The Astrophysical Journal, 799:156 (23pp), 2015 February 1 doi:10.1088/0004-637X/799/2/156

SULFUR ISOTOPIC COMPOSITIONS OF SUBMICROMETER SiC GRAINS FROM THE MURCHISON METEORITE

Yuchen Xu[1,2,7], Ernst Zinner[2], Roberto Gallino[3], Alexander Heger[4,8], Marco Pignatari[5,8], and Yangting Lin[6]
[1] Institute of Geochemistry, Chinese Academy of Sciences, Guiyang 550002, China; xuyuchen@mail.iggcas.ac.cn
[2] Laboratory for Space Sciences and Physics Department, Washington University, St. Louis, MO 63130, USA
[3] Dipartimento di Fisica, Università di Torino, I-10125 Torino, Italy
[4] Monash Centre for Astrophysics, School of Mathematical Sciences, Monash University, Vic 3800, Australia
[5] Department of Physics, University of Basel, CH-4056 Basel, Switzerland
[6] Key Laboratory of Earth's Deep Interior, Institute of Geology and Geophysics, Chinese Academy of Sciences, Beijing 100029, China
Received 2014 February 13; accepted 2014 November 19; published 2015 January 27

ABSTRACT

We report C, Si, N, S, Mg–Al, and Ca–Ti isotopic compositions of presolar silicon carbide (SiC) grains from the SiC-rich KJE size fraction (0.5–0.8 μm) of the Murchison meteorite. One thousand one hundred thirteen SiC grains were identified based on their C and Si isotopic ratios. Mainstream, AB, C, X, Y, and Z subtypes of SiC, and X-type silicon nitride (Si_3N_4) account for 81.4%, 5.7%, 0.1%, 1.5%, 5.8%, 4.9%, and 0.4%, respectively. Twenty-five grains with unusual Si isotopic ratios, including one C grain, 16 X grains, 1 Y grain, 5 Z grains, and 2 X-type Si_3N_4 grains were selected for N, S, Mg–Al, and Ca–Ti isotopic analysis. The C grain is highly enriched in ^{29}Si and ^{30}Si (δ^{29}Si $= 1345‰ \pm 19‰$, δ^{30}Si $= 1272‰ \pm 19‰$). It has a huge ^{32}S excess, larger than any seen before, and larger than that predicted for the Si/S supernova (SN) zone, providing evidence against the elemental fractionation model by Hoppe et al. Two SN models investigated here present a more satisfying explanation in terms of a radiogenic origin of ^{32}S from the decay of short-lived ^{32}Si ($\tau_{1/2} = 153$ yr). Silicon-32 as well as ^{29}Si and ^{30}Si can be produced in SNe by short neutron bursts; evidence for initial ^{44}Ti ($\tau_{1/2} = 60$ yr) in the C grain is additional evidence for an SN origin. The X grains have marginal ^{32}S excesses, much smaller than expected from their large ^{28}Si excesses. Similarly, the Y and Z grains do not show the S-isotopic anomalies expected from their large Si isotopic anomalies. Low intrinsic S contents and contamination with isotopically normal S are the most likely explanations.

Key words: astrochemistry – circumstellar matter – nuclear reactions, nucleosynthesis, abundances – supernovae: general – stars: AGB and post-AGB

1. INTRODUCTION

Stardust grains, also called presolar grains, formed in stellar outflows from late-type stars or in ejecta from stellar explosions before the formation of the solar system some 4.6 Gyr ago, and survived their interstellar journey into the solar system (Lodders & Amari 2005; Zinner 2014). They have been identified in meteorites (e.g., Amari et al. 1994; Huss & Lewis 1995), interplanetary dust particles (Messenger et al. 2003), Antarctic micrometeorites (Yada et al. 2008), and cometary matter (Stadermann et al. 2008) based on their anomalous isotopic compositions (Clayton & Nittler 2004; Zinner 2014). The laboratory study of presolar grains can provide new information on stellar nucleosynthesis (setting constraints on theoretical models), galactic chemical evolution, mixing of ejecta during and after supernova (SN) explosions, and grain formation in circumstellar environments.

Presolar grains of SiC, the best-studied presolar mineral phase, are divided into distinct groups, based on their C-, N-, and Si-isotopic compositions: mainstream, AB, X, Y, Z, possible Nova grains, and C and U grains (Nittler 2003; Clayton & Nittler 2004; Davis 2011; Zinner 2014). Asymptotic giant branch (AGB) stars and core–collapse SNe are the main two sources of stardust. Most presolar SiC grains formed in the winds of 1–3 $M_\odot$ AGB stars (Lugaro et al. 2003), mainstream grains from stars of close-to-solar metallicity, while Y and Z grains from stars of lower-than-solar metallicity (Amari et al. 2001; Zinner et al. 2006, 2007). X grains, C grains, and X-type Si_3N_4 are believed to come from core–collapse SNe (SNe II) based on their Si isotopic anomalies and high inferred initial ^{26}Al/^{27}Al and ^{44}Ti/^{48}Ti ratios (Hoppe et al. 2012; Lin et al. 2010; Pignatari et al. 2013b, 2013c). Type X SiC grains and X-type Si_3N_4 grains have large ^{28}Si excesses, whereas C grains have large ^{29}Si and ^{30}Si excesses. All SN SiC grains are extremely rare: X grains account for 1% of all presolar SiC grains, C grains and Si_3N_4 grains for only ~0.1%. Most of them were found during automatic searches for rare grains with the ion microprobe.

Besides the major elements C and Si, many other elements have been analyzed for their isotopic ratios in SiC grains (Hynes & Gyngard 2009). Sulfur isotopic measurements have been made only recently. These measurements revealed large ^{32}S excesses in C grains (Gyngard et al. 2010a; Hoppe et al. 2012) and smaller ^{32}S excesses in X grains (Hoppe et al. 2012) and U grains (Hoppe et al. 2012; Orthous-Daunay et al. 2012). Type U grains, like C grains, have large ^{29}Si and ^{30}Si excesses, but, in contrast, have low ^{12}C/^{13}C ratios of less than 10.

Here we report the results of C, Si N, S, Mg–Al, and Ca–Ti isotopic measurements of selected presolar SiC grains from the SiC-rich KJE size fraction (0.5–0.8 μm) of the Murchison meteorite (Amari et al. 1994), with emphasis on the S isotopic ratios of the grains. Grains of type C, X, Y, and Z were identified from an automatic grain search. In Section 2 we describe the experimental measurements, in Section 3 we report the results

[7] Institute of Geology and Geophysics, Chinese Academy of Sciences, No. 19, Bei Tucheng Xilu, Chaoyang District, Beijing 100029, China.
[8] NuGrid Collaboration, http://www.nugridstars.org

and discuss their implications in terms of stellar models. This is followed by conclusions in Section 4. Preliminary results have been reported by Xu et al. (2012).

2. EXPERIMENTAL PROCEDURES

The details of the chemical and physical separation of presolar SiC grains from the Murchison carbonaceous meteorite have been described by Amari et al. (1994). KJE is the SiC-rich size fraction with nominal diameters between 0.5 and 0.8 μm. In this work, a search for rare SiC grains was undertaken by automatic isotopic imaging in the auto-grain mode with the Cameca NanoSIMS 50 ion microprobe at Washington University (Gyngard et al. 2010b). Thousands of KJE SiC grains were deposited from liquid suspension onto a clean gold foil. Prior to ion imaging, the analyzed areas were bombarded with a high-current Cs^+ ion beam for cleaning and implantation of Cs. Approximately 25 nm were removed in this step. Simultaneous ion images of $^{12}C^-$, $^{13}C^-$, $^{28}Si^-$, $^{29}Si^-$, and $^{30}Si^-$ were acquired by rastering a focused Cs^+ ion beam ($\sim$1 pA, 100 nm) over areas $40 \times 40\ \mu m^2$ in size. SiC grains were identified by an automatic grain-recognition algorithm. These grains were analyzed in detail by deflecting the primary Cs^+ beam onto individual grains and rastering the beam over square areas 1.5–2 times the grain diameter on a side. Subsequently, the sample stage was moved to an adjacent analysis area and the process was repeated.

Out of a total number of 1113 SiC grains we identified 906 mainstream grains, 63 AB grains, 1 C grain, 17 X grains, 64 Y grains, 55 Z grains, 2 nova grain candidates, and 5 X-type Si_3N_4 grains. Out of these we measured N and S isotopic ratios in 1 C grain, 16 X grains, and 2 Si_3N_4 grains. We also selected one Y grain and five Z grains with the largest ^{30}Si excesses for such isotopic analyses. These measurements were made by obtaining negative ion images of $^{12}C^{14}N^-$, $^{12}C^{15}N^-$, $^{32}S^-$, $^{33}S^-$, and $^{34}S^-$ in multi-collection mode by rastering the Cs^+ beam over 2×2 to $3 \times 3\ \mu m^2$ areas covering the grains. From the images we obtained $^{14}N/^{15}N$ ratios and $\delta^{33}S/^{32}S$ and $\delta^{34}S/^{32}S$ values (δ-values are deviations from normal isotopic ratios in parts per thousand). The advantage of the imaging mode is that it allows us to exclude contributions from other attached or nearby SiC grains to the N and S signals from the measured grains. A synthetic SiC–Si_3N_4 mix was used for N as standard. For S we used FeS and the S signal from the SiC–Si_3N_4 mix that contained enough S. Since S in FeS is a main element, but a trace element in the SiC–Si_3N_4 mix, this allowed us to study the QSA (Quasi-Simultaneous Arrival) effect for S (Slodzian et al. 2004; see also Gyngard et al. 2009). The analyses of Al–Mg and Ti–Ca were made with positive secondary ions produced with an O^- primary beam. ^{24}Mg, ^{25}Mg, ^{26}Mg, ^{27}Al, and ^{28}Si were measured in multi-collection mode by rastering the primary O^- beam of $\sim$10 pA over small areas around one C grain, 1 Si_3N_4 grain, and 13 X grains. Subsequently, these grains were measured for ^{28}Si, ^{40}Ca, ^{42}Ca, ^{44}Ca, and ^{48}Ti, also in multi-collection mode. Terrestrial spinel was used as a standard for Mg and Al, and perovskite ($CaTiO_3$) for the isotopes of Ca and Ti. The sensitivity factors obtained were $Al^+/Mg^+ = 1.78 \times$ Al/Mg and $Ca^+/Ti^+ = 2.83 \times$ Ca/Ti.

3. RESULTS AND DISCUSSION: GRAIN DATA AND SN MIXING MODELS

The isotopic compositions of the 25 grains selected for detailed isotopic analysis are given in Table 1. The C, N, inferred $^{26}Al/^{27}Al$ and $^{44}Ti/^{48}Ti$ ratios for C grains, X grains, U grains, and X-type Si_3N_4 grains, including data from previous studies, are given in Figures 1 and 2. Figures 3(a)–(c) present plots of the Si and S isotopic ratios of the grains of this study as well as of C, U, X, Y, and Z grains of previous studies in which S isotopic ratios had been measured (Gyngard et al. 2010a, 2012; Hoppe et al. 2012; Orthous-Daunay et al. 2012). The $\delta^{30}Si/^{28}Si$ values and inferred $^{32}Si/^{28}Si$ ratios for C and U grains are given in Figure 4. All grains believed to have an SN origin (C, X, Si_3N_4) as well as U grains show low $^{14}N/^{15}N$ ratios (^{15}N excesses) but a large range of $^{12}C/^{13}C$ ratios (Figure 1). All grains measured for Al–Mg show large ^{26}Mg excesses due to the decay of short-lived ($\tau_{1/2} = 7.2\times10^5$ yr) ^{26}Al (Table 1). The table gives the $^{26}Al/^{27}Al$ ratios inferred from ^{26}Mg excesses. The C grain and four X grains have large ^{44}Ca excesses resulting from the decay of short-lived ($\tau_{1/2} = 60$ yr) ^{44}Ti. Because ^{44}Ti is produced only in SNe (Timmes et al. 1996; Magkotsios et al. 2010), its initial presence is evidence for an SN origin of these grains. The table gives inferred $^{44}Ti/^{48}Ti$ ratios. Figures 2(a) and (b) show the inferred $^{26}Al/^{27}Al$ and inferred $^{44}Ti/^{48}Ti$ ratios of the C grains and X grains of this and previous studies plotted against their $^{12}C/^{13}C$ ratios.

Before we discuss the S isotopic ratios of the grains of this study in more detail, we want to emphasize two fundamental problems with S isotopic measurements in presolar SiC grains: first, S does not readily condense into SiC and intrinsic S concentrations are very low and, second, contamination with isotopically normal S is ubiquitous. One reason for the latter is that the SiC-rich residue has been treated with sulfuric acid to dissolve spinel grains (Amari et al. 1994), another reason is the mobile nature of S and its compounds. The contamination problem is demonstrated in Figures 5 and 14–17, which show negative ion isotopic images of S and CN and secondary electron images of the C Grain a1–5–7 and four X grains. As can be seen in Figure 5, most of the S, especially ^{33}S and ^{34}S, is located at the periphery of the grain. If we use the whole image, we obtain $\delta^{33}S/^{32}S = -714‰ \pm 24‰$, and $\delta^{34}S/^{32}S = -703‰ \pm 14‰$, whereas from the selected area outlined in the images we obtain $\delta^{33}S/^{32}S = -944‰ \pm 33‰$, and $\delta^{34}S/^{32}S = -941‰ \pm 14‰$. It is clear that the selected area is almost completely devoid of ^{33}S and ^{34}S, while the intrinsic S is dominated by ^{32}S. Below we will discuss the S contamination problem in more detail.

3.1. *Type C Grains and Their Stellar Sources*

The C grain of this study, a1–5–7, has extreme excesses in ^{29}Si and ^{30}Si ($\delta^{29}Si/^{28}Si = 1345‰ \pm 19‰$, $\delta^{30}Si/^{28}Si = 1272‰ \pm 19‰$; Table 1; Figure 3(a)). Whereas models predict large ^{30}Si excesses for AGB stars of low metallicity, these excesses are expected to be accompanied by ^{29}Si deficits (Zinner et al. 2006); such isotopic patterns are found in SiC grains of type Z (Table 1). In contrast, large excesses in both ^{29}Si and ^{30}Si are predicted for certain zones in core–collapse SNe, e.g., in part of the He/C zone (e.g., Woosley & Weaver 1995; Rauscher et al. 2002; Woosley & Heger 2007). Grain a1–5–7 carries this isotopic signature together with C and N isotopic ratios of $^{12}C/^{13}C$ = 192 and $^{14}N/^{15}N = 58$ (Figure 1), similar to those observed in SiC X grains, believed to have an SN origin (e.g., Lin et al. 2010). The inferred $^{26}Al/^{27}Al$ ratio of this grain is 1.7×10^{-3}, not high enough to provide definitive proof of an SN origin. Such proof, however, is provided by evidence for the initial presence of ^{44}Ti with $^{44}Ti/^{48}Ti = 4.2 \times 10^{-2}$.

Grain a1–5–7 has the largest ^{33,34}S depletions (or ^{32}S excess) observed in any C grain (Figure 3(b)). The Si and S isotopic ratios in C grains have posed a puzzle, because in SNe

Table 1
Isotopic Compositions of Selected Grains

Grain Label	Type	$^{12}C/^{13}C$	$^{14}N/^{15}N$	$\delta^{29}Si/^{28}Si$ (‰)	$\delta^{30}Si/^{28}Si$ (‰)	$\delta^{25}Mg/^{24}Mg$ (‰)	$\delta^{26}Mg/^{24}Mg$ (‰)	$^{26}Al/^{27}Al$ (×1000)
KJE-a1–5–7	C	192.0 ± 1.1	58.4 ± 2.2	1345 ± 19	1272 ± 19	−172 ± 167	2625 ± 394	1.7 ± 0.1
KJE-a1–3–2	Si_3N_4	7.9 ± 0.1	4.5 ± 0.2	−434 ± 5	−317 ± 6			
KJE-C-Si-6–13	Si_3N_4	90.6 ± 1.2	53.8 ± 2.0	−138 ± 7	−271 ± 6	0 ± 117	230047 ± 9668	107.3 ± 4.0
KJE-a1–20–7	X	100.8 ± 0.5	62.3 ± 2.3	−194 ± 6	−330 ± 6	−59 ± 115	2429325 ± 101740	422.7 ± 15.6
KJE-a1–22–4	X	26.7 ± 0.1	36.3 ± 1.3	−137 ± 7	−161 ± 7	131 ± 90	917412 ± 28389	269.3 ± 9.9
KJE−a1–33–7	X	234.8 ± 1.4	187.2 ± 8.1	−683 ± 3	−501 ± 4	−95 ± 93	860372 ± 30540	332.7 ± 12.2
KJE-a1–37–7	X	145.2 ± 0.8	128.5 ± 4.7	−601 ± 3	−528 ± 4			
KJE-a1–42–3	X	63.3 ± 0.3	75.6 ± 2.8	−94 ± 7	−171 ± 7	62 ± 127	674523 ± 29290	175.1 ± 6.4
KJE-a1–45–8	X	1694 ± 21	63.2 ± 2.5	−588 ± 3	−605 ± 3	13 ± 65	227736 ± 5770	236.4 ± 8.7
KJE-a1–48–1	X	50.2 ± 0.2	107.1 ± 4.3	−360 ± 5	−359 ± 5	123 ± 152	309397 ± 15545	53.2 ± 2.0
KJE-a1–5–20	X	41.7 ± 0.3	116.2 ± 4.7	−188 ± 7	−279 ± 7			
KJE-a1–6–18	X	2377 ± 28	18.5 ± 0.8	−555 ± 4	−694 ± 3	−19 ± 107	1275534 ± 48995	435.7 ± 16.0
KJE-a2–10–3	X	56.9 ± 0.5	167.2± 7.6	−168 ± 8	−142 ± 9			
KJE-a2–13–4	X	2510 ± 85	38.3 ± 1.4	−337 ± 6	−582 ± 4	−42 ± 239	442249 ± 37151	210.6 ± 7.7
KJE-a2–14–8	X	3101 ± 116	28.2 ± 1.1	−521 ± 4	−467 ± 5	−333 ± 209	2564343 ± 227535	437.0 ± 16.1
KJE-a2–28–7	X	693.4 ± 9.2	124.4 ± 4.7	−382 ± 5	−553 ± 4	−22 ± 180	139866 ± 9032	119.2 ± 4.4
KJE-a2–44–1	X	1550 ± 30	60.0 ± 2.2	−381 ± 5	−589 ± 4	327 ± 254	3888531 ± 286597	471.3 ± 17.3
KJE-a2–45–9	X	129.6 ±0.8	72.7 ± 2.0	−204 ± 7	−378 ± 5	−13 ± 114	515823 ± 21097	171.9 ± 6.3
KJE-a2–6–6	X	75.4 ± 0.5	68.8 ± 2.6	−155 ± 7	−273 ± 7	−58 ± 46	36054 ± 792	66.2 ± 2.4
KJE-a1–16–11	Y	115.4 ± 0.7	3569± 402	−154 ± 7	874 ± 16			
KJE-a1–17–4	Z	48.6 ± 0.3	1130 ± 33	−129 ± 7	333 ± 11			
KJE-a1–17–8	Z	65.5 ± 0.3	3032 ± 127	−124 ±7	237 ± 10			
KJE-a1–37–6	Z	94.4 ± 0.6	1248 ± 59	−131 ± 7	354 ± 12			
KJE-a2–27–2	Z	50.2 ± 0.3	1962 ± 281	−119 ± 8	296 ± 12			
KJE-a2–5–16	Z	87.2 ± 0.5	2134±104	−132 ± 7	321 ± 11			

Grain Label	Type	$\delta^{33}S/^{32}S$ (‰)	$\delta^{34}S/^{32}S$ (‰)	$\delta^{42}Ca/^{40}Ca$ (‰)	$\delta^{44}Ca/^{40}Ca$ (‰)	$^{44}Ti/^{48}Ti$ (×1000)	S/Si (×1000)
KJE-a1–5–7	C	−944 ± 33	−941 ± 14	403 ± 449	947 ± 213	42.2 ± 9.2	5.4
KJE-a1–3–2	Si_3N_4	−83 ± 121	−67 ± 51				5.9
KJE-C-Si-6–13	Si_3N_4	−18 ± 37	−39 ± 15	167 ± 36	25 ± 22		5.8
KJE-a1–20–7	X	−65 ± 38	−56 ± 16	50 ± 157	−28 ± 91		5.8
KJE-a1–22–4	X	−87 ± 61	−56 ± 24	52 ± 73	149 ± 39	22.9 ± 2.5	38.9
KJE-a1–33–7	X	−47 ± 107	−128 ± 43	−85 ± 117	17676 ± 17	213.2 ± 4.0	9.2
KJE-a1–37–7	X	2 ± 30	−23 ± 13	−34 ± 71	87 ± 38	5.9 ± 0.8	47.3
KJE-a1–42–3	X	−137 ± 57	−46 ± 25	−157 ± 234	32 ± 123		11.0
KJE-a1–45–8	X	−1 ±71	−44 ± 29	5 ± 133	74 ± 72		23.5
KJE-a1–48–1	X	182 ± 159	−124 ± 57	119 ± 95	9 ± 56		2.6
KJE-a1–5–20	X	123 ± 281	168 ± 120				115.6
KJE-a1–6–18	X	−155 ± 126	−82 ± 55	411 ± 135	248 ± 80		15.0
KJE-a2–10–3	X	−400 ± 155	−179 ± 76				23.0
KJE-a2–13–4	X	12 ± 72	−50 ± 29	608 ± 279	−129 ± 210		12.4
KJE-a2–14–8	X	−104 ± 59	−80 ± 25	−84 ± 449	346 ± 207		16.7
KJE-a2–28–7	X	−144 ± 39	−72 ± 17	326 ± 449	1190 ± 197	118.0 ± 35.6	129.7
KJE-a2–44–1	X	−47 ± 208	−141 ± 83	−43 ± 334	269 ± 162		8.8
KJE-a2–45–9	X	−249 ± 109	−120 ± 49	49 ± 303	293 ± 153		8.9
KJE-a2–6–6	X	281 ± 151	−53 ± 54				6.9
KJE-a1–16–11	Y	−5 ± 65	34 ± 28				3.3
KJE-a1–17–4	Z	42 ± 28	−90 ± 11				55.6
KJE-a1–17–8	Z	21 ± 33	−7 ± 14				14.4
KJE-a1–37–6	Z	−42 ± 41	−31 ± 17				15.2
KJE-a2–27–2	Z	−44 ± 87	−41 ± 37				8.7
KJE-a2–5–16	Z	−39 ± 58	−12 ± 25				13.9

Notes. The errors of all data reported are 1σ. The names of grains are composed of three parts according to the auto-grain steps. The letter "a" stands for "area," using "a1" and "a2" for short. Taking "KJE-a1_5_7" for example, this grain was found in area 1 (the area analyzed first), the seventh grain identified in sub-area 5 by the auto-grain software based on the Si signal.

$^{29,30}Si/^{28}Si$ and $^{33,34}S/^{32}S$ ratios are positively correlated (Rauscher et al. 2002; Woosley & Heger 2007). The Si/S zone is the only SN zone with large ^{32}S excesses, but it also has large ^{28}Si excesses and, vice versa, large $^{33,34}S$ excesses are predicted for regions with large $^{29,30}Si$ excesses. Hoppe et al. (2012) invoked elemental fraction between Si and S by assuming that in C grains S is dominated by contributions from the Si/S zone, while Si is dominated by contributions from outer zones with

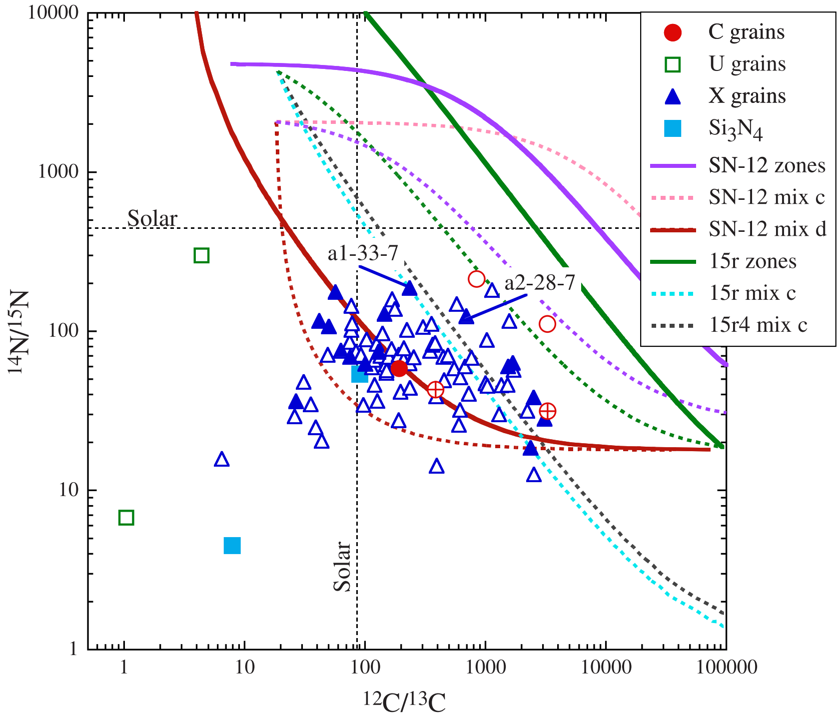

Figure 1. Nitrogen isotopic ratios of different types of rare presolar SiC grains and Si_3N_4 grains are plotted against their C isotopic ratios. In this and subsequent figures grains of this study are plotted as solid symbols, grains previously analyzed by other investigators (http://presolar.wustl.edu/~pgd) are plotted as open symbols. Type C grains with crosses are grains whose S isotopic ratios have been measured. Also plotted are different mixing lines resulting from mixing either whole zones or individual layers from the 12 $M_\odot$ SN model by Woosley & Heger (2007) and the 15r and 15r4 models by Pignatari et al. (2013c). Solid lines are for mixtures between the He/C (C/O + He/C for the 12 $M_\odot$ SN model) zone and the He/N zone or between layers therein, broken lines for mixtures between the He/C (C/O + He/C) zone and the H envelope. The letters c and d refer to the layers shown in Figure 7. Two selected X grains of this study are labeled.

isotopically heavy Si. This explanation is completely ad hoc and the fractionation process is not understood at all. More importantly, grain a1–5–7 provides proof against this interpretation. The reason is that the S isotopic composition of this grain is more ^{32}S-rich than the average of the Si/S zone, e.g., in the 15 $M_\odot$ SN model by Rauscher et al. (2002) and other SN models (see Figure 3(b)). Figure 6 shows this in more detail for several SN models. Plotted are the predicted S isotopic ratios for the Si/S zones of the 12 $M_\odot$ core–collapse SN model by Woosley & Heger (2007) and the 15, 20, and 25 $M_\odot$ SN models by Rauscher et al. (2002), as well as the average ratios of the whole Si/S zones. As can be seen, the predicted ratios do not reach those of grain a1–5–7. A much more satisfying explanation, proposed by Pignatari et al. (2013c), is that the ^{32}S excess in C grains is of radiogenic origin from the decay of short-lived ^{32}Si ($\tau_{1/2}$ = 153 yr). In this model, both, the large ^{29,30}Si excesses and large ^{32}S excess are produced by the same process.

Silicon-32 is produced by neutron capture. Because ^{31}Si has a short half life ($\tau_{1/2}$ = 2.6 hr), the production of ^{32}Si requires high neutron densities. Such high neutron densities can be found inside of SNe in the outer layers of the O/C zone or at the bottom of the He/C zone, produced by the $^{22}Ne(\alpha, n)^{25}Mg$ reaction that is activated by the passage of the SN shock. This is the so-called *n*-process (Blake & Schramm 1976), causing a short neutron burst, which has been proposed by Meyer et al. (2000) to be responsible for the Mo isotopic pattern found in X grains (Pellin et al. 1999). An alternative model to explain the Mo isotopic pattern in X grains has been proposed by Farouqi et al. (2009). In this model the Mo isotopes are produced by charged particles (mostly α particles) in the high-entropy wind of Type II SNe. However, it still needs to be seen whether a mixing model including the component of the neutrino-wind ejecta can produce large ^{29}Si, ^{30}Si excesses, and large amounts of ^{32}Si. Since the two core–collapse SN models adopted for comparison with the presolar grain data do not include the neutrino-wind ejecta, we concentrate on the neutron burst models in the C-rich He shell. In the 15 $M_\odot$ SN model by Rauscher et al. (2002) and in models with higher mass, such a neutron burst and the resulting Mo isotopic pattern is found in the outer layers of the O/C zone. These layers have also a high abundance of ^{32}Si (as well as large ^{29}Si and ^{30}Si excesses). This region, however, is O-rich, and therefore not conducive for the condensation of SiC. More promising is the 12 $M_\odot$ SN model by Woosley & Heger (2007),[9] where a ^{32}Si-rich layer with large ^{29}Si and ^{30}Si excesses is located in a C-rich region, right at the boundary between the C/O and He/C zones (Figure 8(a)). A ^{32}Si-rich zone is also found in the 15 $M_\odot$ core–collapse SN model by Pignatari et al. (2013c). In this model, at high shock velocities the ensuing high temperatures result in efficient α-capture at the bottom of the He/C zone, forming the C/Si zone. High neutron densities, ranging up to 10^{22} cm^{-3}, in layers outside of the C/Si zone, produce high ^{32}Si abundances and large ^{29,30}Si excesses (Figure 8(b)). The authors demonstrated that their model can produce sufficiently high $^{32}Si/^{28}Si$ ratios to explain the S isotopic compositions measured in C grains. They did not consider the C, N, Al, and Ti isotopic ratios of the grains, however. In the ^{32}Si-rich regions of both the 12 $M_\odot$ SN and 15 $M_\odot$ SN model C consist of almost pure ^{12}C, the result of He burning. In order to produce the C isotopic ratios observed in the C grains, we assume that before grain condensation extensive mixing took place between the ^{12}C- and ^{32}Si-rich He/C zone and

[9] Available at: http://2sn.org/sollo03

the He/N zone and/or the H-rich envelope, both characterized by low $^{12}C/^{13}C$ ratios, the result of H burning in the CNO cycle during previous stellar evolutionary stages.

In order to test these assumptions, different layers of the SN ejecta are mixed. This procedure is justified since astronomical observations of SN remnants have shown a large degree of mixing and asymmetries of the ejected material (e.g., Grefenstette et al. 2014). While these stars were obviously not the source of the presolar grains found in meteorites, we assume that the same type of mixing occurred in the old parent SNe, with the most relevant constraint for the formation of carbide grains being that the resulting mixture has C/O > 1 (e.g., Travaglio et al. 1999; Yoshida 2007).

Therefore, in order to compare presolar grain measurements with stellar models, we performed mixing calculations between different regions for the 12 $M_\odot$ SN model and the Pignatari et al. (2013c) models 15r and 15r4, the 15r model having the highest explosion energy and temperature. The 15r model is based on the analytical prescription by Fryer et al. (2012). The 15r4 model has a shock velocity lower by a factor of four than the shock velocity of the 15r model (Pignatari et al. 2013a). First, we mixed the whole C/O + He/C zone with the entire He/N zone of the Woosley & Heger (2007) model and the whole He/C zone with the entire He/N zone of the Pignatari et al. models. We also mixed individual layers in the C/O and He/C zone with layers in the He/N zone for the three models. In addition, we also mixed zones and layers from the He/C (O/C + HeC) zone with the H envelope. The relevant zones and the individual layers for the models are indicated in Figure 8. In these mixing calculations the relative proportions of the two constituents of the mix have been varied, resulting in the curves shown in Figure 4, which are compared with the $^{30}Si/^{28}Si$ ratios and inferred $^{32}Si/^{28}Si$ ratios of grain a1–5–7 and other C grains. Also plotted are U grains, which have the same Si and S isotopic signatures as C grains but have much smaller $^{12}C/^{13}C$ ratios. In Figure 4(a) it can be seen that the full-zone mixture of the 12 $M_\odot$ SN model misses most of the C grains. Even SN-12 mix a, which mixes the layer with the maximum $^{30}Si/^{28}Si$ ratios and $^{32}Si/^{28}Si$ ratios (Figure 8(a)) with a layer in the He/N zone or the H envelope and which therefore produces the largest $^{30}Si/^{28}Si$ ratios for a given $^{12}C/^{13}C$ ratio in the mix, cannot account for the isotopic ratios of a1–5–7 and most other C grains.

As can be seen from the plots in Figure 4(a), mixing with the H envelope produces mixing lines that are shifted to the left, i.e., have smaller $^{12}C/^{13}C$ ratios, from the mixing lines with the He/N zone. This seems to be counter-intuitive because the He/N zone has lower $^{12}C/^{13}C$ ratios than the H envelope. The reason is that in such mixing calculations it is not only the isotopic ratio but also the absolute abundances of the isotopes in question that matter. The H envelope has much higher abundances of the C isotopes than the He/N zone. An extreme example of this principle is shown in some mixing curves in Figure 1. This figure shows a mixing curve between layer d at internal mass 2.31 $M_\odot$ in the He/C zone with a layer at mass 3.185 $M_\odot$ in the H envelope in the 12 $M_\odot$ SN model. Layer d is the layer where ^{15}N reaches a maximum (Figure 7(a)). This mixing curve reaches low $^{14}N/^{15}N$ ratios for a range of $^{12}C/^{13}C$ ratios and falls below all the C grains and most X grains (Figure 1). Compare this with the SN-12 mix c curve between layer c and the same layer in the H envelope. In layer c the $^{14}N/^{15}N$ ratio is much higher than in layer d, but the ^{15}N abundance is much lower. The resulting curve has very high $^{14}N/^{15}N$ ratios up to very high $^{12}C/^{13}C$ ratios and misses all

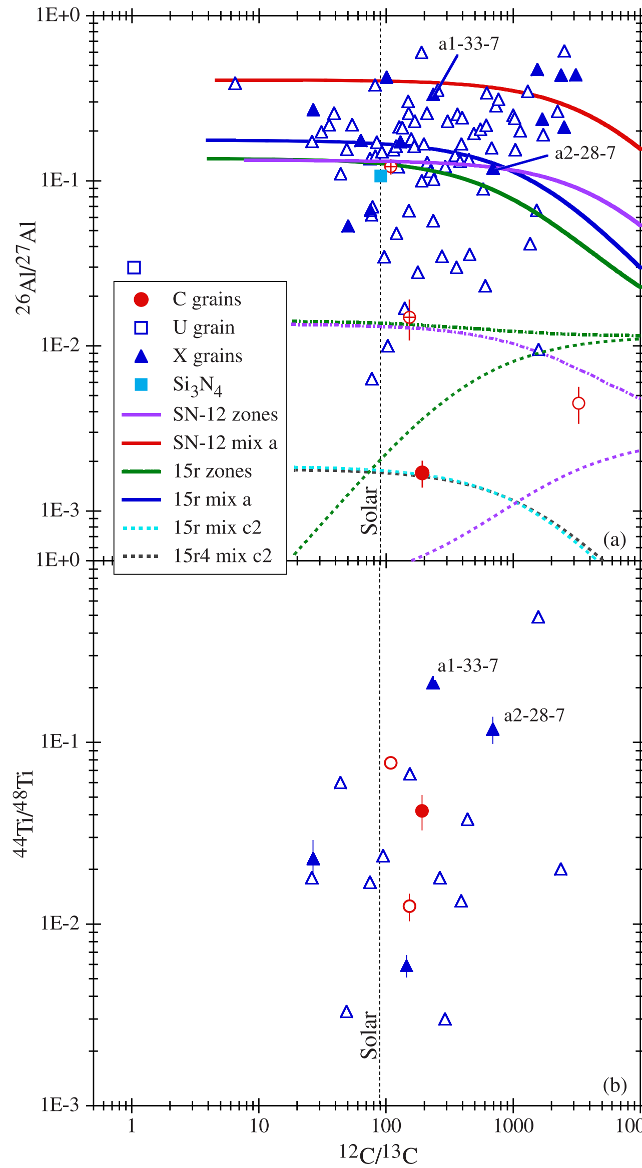

Figure 2. (a) Inferred initial $^{26}Al/^{27}Al$ ratios of different rare types of presolar SiC grains are plotted against their $^{12}C/^{13}C$ ratios. As in Figure 1, solid mixing lines are between the He/C (C/O + He/C for the 12 $M_\odot$ SN model) zone and the He/N zone or between layers therein, broken lines for mixtures between the He/C (C/O + He/C) zone and the H envelope. Dash-dotted lines are between the He/C (C/O + He/C) zone and a 1:1 mixture of the He/N zone and H envelope for the 12 $M_\odot$ SN model and a 2:1 mixture of the He/N zone and H envelope for the 15r model. Line 15r and 15r4 mix c2 are between layer c at 3.488 (model 15r) or 3.307 (model 15r4) internal mass and a 0.0063:0.9937 mix between layers at mass 4.758 (He/N zone) and mass 4.87 (H envelope). (b) Inferred initial $^{44}Ti/^{48}Ti$ ratios of C and X grains are plotted against their $^{12}C/^{13}C$ ratios.

the grains. Another examples are the a and b mixing curves of the 15r SN model (Figure 4(a)). Mix b has higher $\delta^{30}Si/^{28}Si$ values than mix a although the $^{30}Si/^{28}Si$ ratio is higher in layer a (Figure 8(b)).

In contrast to the failure of mixing lines from the 12 $M_\odot$ SN model to match C grain a1–5–7 in Figure 4(a), the full-zone mixing line of model 15r for the $^{32}Si/^{28}Si$ versus $^{12}C/^{13}C$ plot is close to the isotopic ratios of a1–5–7 and mixing of different layers of the He/C zone for both the 15r and 15r4 models (Figure 4(a)) with a He/N layer and/or a H envelope layer can cover all grains. The grains to the right of the 15r and 15r4 lines with the highest $^{12}C/^{13}C$ can be reached by selecting a layer

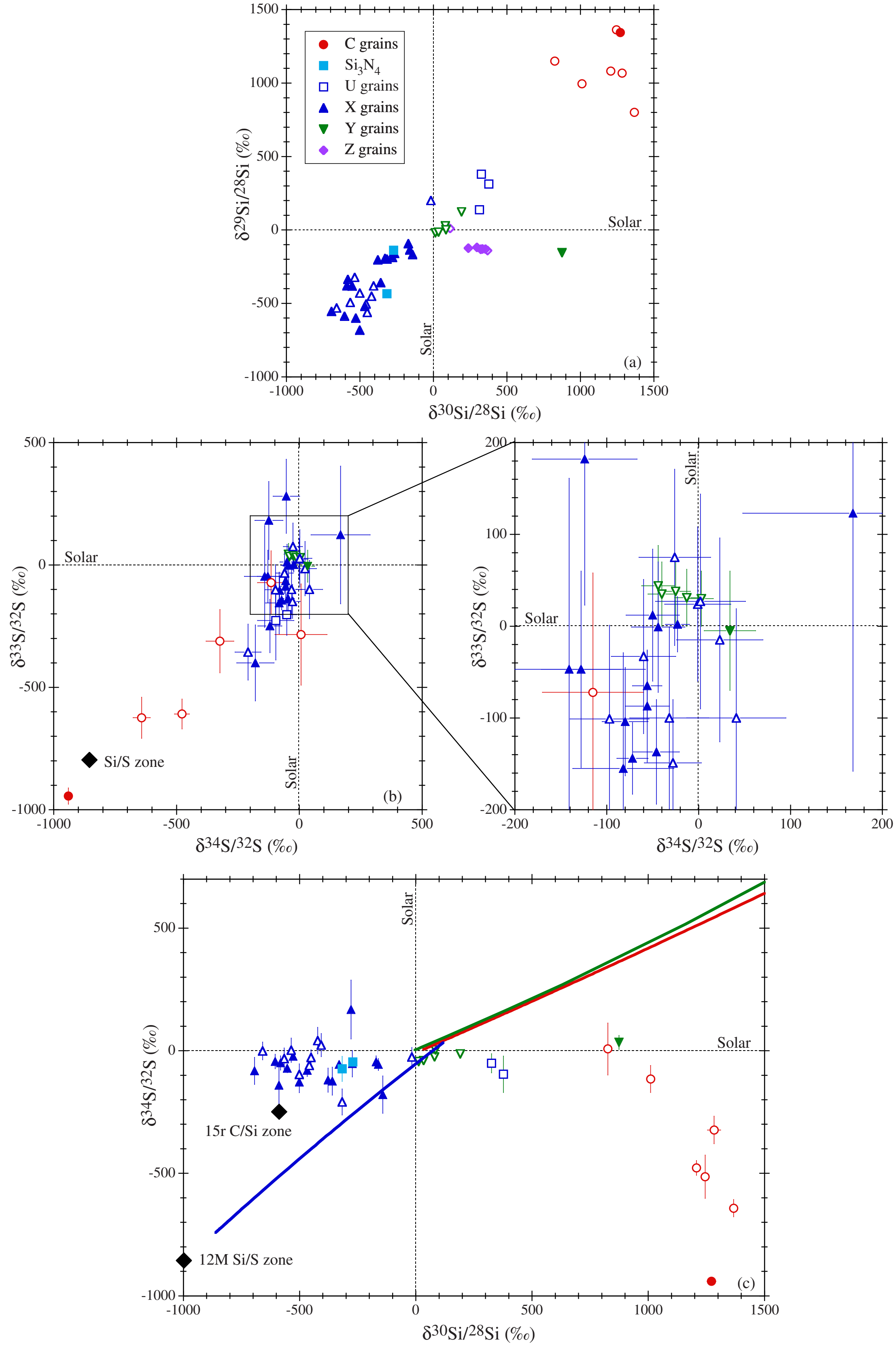

Figure 3. Silicon and sulfur isotopic compositions of different types of rare presolar SiC grains. Si and S isotopic of the SiC grains in all plots are given as δ-values, deviations from the solar ratios in permil (‰). (a) Si isotopic ratios of selected SiC grains. (b) S isotopic ratios of selected rare SiC grains. The average S isotopic ratios of the S/Si zone of the 15 $M_{\odot}$ SN model by Rauscher et al. (2002) are indicated. (c) $\delta^{34}S/^{32}S$ values of grains are plotted against their $\delta^{30}Si/^{28}Si$ values. The ratios of the S/Si zone of the 15 $M_{\odot}$ SN model by Rauscher et al. (2002) and those of the C/Si zone of the 15r model by Pignatari et al. (2013b) are depicted by solid diamonds. The two solid lines in the right upper quadrant are mixing lines between the C/O-He/C and He/N zones of the 12 $M_{\odot}$ SN model by Woosley & Heger (2007; lower line) and between the He/C and He/N zones of the 15r model by Pignatari et al. (2013c). The solid line in the left lower quadrant is a mixing line between the Si/S zone and a mix between the He/C and He/N zones of the 15 $M_{\odot}$ SN model by Rauscher et al. (2002). In all figures errors are 1σ.

with higher internal mass that has lower $^{29,30}Si/^{28}Si$ ratios but still a high $^{12}C/^{13}C$ ratio (to the right of layer c in (Figure 8(b)).

Figure 4(b) shows that mix a of the 12 $M_\odot$ SN model can reproduce the inferred $^{32}Si/^{28}Si$ ratio of grain a1–5–7, and all grains can be covered by the right choice of mixtures for this model. Because Si and S isotopes were not measured simultaneously in grain a1–5–7, we estimated the relative ion intensities of both elements from the independent measurements of C and Si isotopes and of N and S isotopes by correcting for differences in primary beam current and raster size. The $^{32}Si/^{28}Si$ ratio was inferred from the $^{32}S/^{28}Si$ ratio and the average of the $\delta^{33}S/^{32}S$ and $\delta^{34}S/^{32}S$ values as explained by Pignatari et al. (2013c) according to the formula

$$^{32}Si/^{28}Si = (^{32}S/^{28}Si) \times (-0.001 \times \delta S),$$

where δS is the average of $\delta^{33}S$ and $\delta^{34}S$. Because the Si and S signals are obtained from the images covering the whole grain, the δ-values $\delta^{33}S/^{32}S = -714‰$, and $\delta^{34}S/^{32}S = -703‰$, and not the ones obtained from the selected area shown in Figure 5 and given in Table 1 have to be taken.

The full-zone mixing line between the He/C and He/N zones of model 15r goes right through the a1–5–7 data point and all grains can be covered by mixing of different individual layers (Figure 4(b)). Pignatari et al. (2013c) explored also models with lower shock velocities and showed that very similar maximum $^{32}Si/^{28}Si$ ratios are obtained down to 1/10 of the shock velocity of model 15r (their Figure 5), which is also shown by the mixing curves for the 15r4 model. In conclusion, the 15r and 15r4 models seem to better explain the Si isotopic ratios of C grains than the 12 $M_\odot$ SN model (Figure 4(a)), but all models can explain the inferred $^{32}Si/^{28}Si$ ratios. The isotopic ratios of the U grains are completely outside of predictions by any baseline SN models and apparently require a different stellar source.

In the models considered here, the regions with ^{32}Si (and large ^{29}Si and ^{30}Si excesses) have heavy S, i.e., large ^{33}S and ^{34}S excesses (see Table 2). In Figure 3(c) the two lines at positive $\delta^{30}Si/^{28}Si$ values are whole-zone mixing lines for the 12 $M_\odot$ and 15r SN models. The fact that the C grains show large ^{34}S deficits instead of excesses means that any indigenous S in the grains must have been completely overwhelmed by radiogenic ^{32}S. We already mentioned that only very little S condensed into SiC. The lower a1–5–7 data point in Figure 13 was obtained by assuming that all the non-radiogenic S in the grain (in the whole image in Figure 5) had normal isotopic composition. However, both SN models predict an excess of ^{34}S of about 600‰. If we assume such a composition then the S/Si ratio for the non-radiogenic S is only 0.001. However, this is only an upper limit because for this estimate we used the full S isotopic image (because the Si signal was obtained from the whole grain) and it is clear that a large portion of ^{34}S is due to contamination and not intrinsic ^{34}S (Figure 5(e)). Pignatari et al. (2013c) assumed a fractionation factor of 10^4 between Si and S during condensation. This is consistent with our estimate. Radiogenic ^{32}S was retained in the SiC grain because it condensed as ^{32}Si. Previous studies of graphite grains have demonstrated that another volatile element, K, is quantitatively retained in graphite if it is radiogenic ^{41}K, produced by the decay of short-lived ^{41}Ca (Zinner & Jadhav 2013).

We can also investigate, how well the SN models match the remaining isotopic ratios in the C grain a1–5–7. Figure 1 shows that zone mixing cannot match the N and C isotopic ratios of the grain but produce $^{14}N/^{15}N$ ratios that are much too high. We have to use layers with high ^{15}N. These are the layer d in the 12 $M_\odot$ SN model and the layer c in the 15r SN model (Figure 7). Mixing with this layer easily covers the N and C isotopic ratios of grain a1–5–7 for the 12 $M_\odot$ SN model. However, a mixture of layer c in the 15r models with a layer in the H envelope still misses grain a1–5–7, although this is the mixture in this model that gets closest to the C and N isotopic ratios of this grain. The mixing curve for layer c with a layer in the H envelope for the 15r4 model is even farther removed from the N and C isotopic ratios of grain a1–5–7.

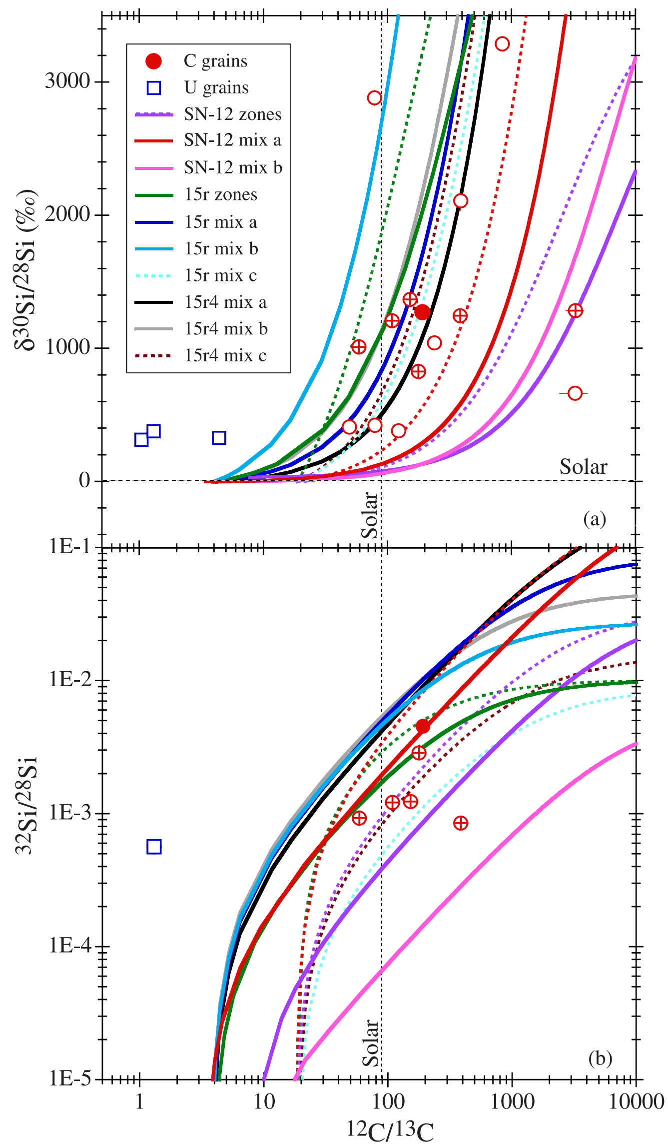

Figure 4. (a) $^{30}Si/^{28}Si$ ratios (expressed as δ-values) of C and U grains are plotted against their $^{12}C/^{13}C$ ratios. The C grain of this study is plotted as a solid sphere. C grains studied previously are plotted as open spheres, those that had their S isotopic ratios analyzed with crossed lines. Also plotted are mixing lines between the C/O–He/C and He/N zones of the 12 $M_\odot$ SN model by Woosley & Heger (2007) and between the He/C and He/N zones of the 15r and 15r4 models by Pignatari et al. (2013c), for the whole zones as well as for individual layers from the He/C and He/N (solid lines) zones and the H envelope (broken lines) as indicated in Figure 7. (b) Inferred (from ^{32}S excesses) $^{32}Si/^{28}Si$ ratios of C and U grains are plotted against their $^{12}C/^{13}C$ ratios. The grain with $^{12}C/^{13}C = 3290$ and $\delta^{30}Si = 1283‰$ in plot (a) is from Gyngard et al. (2010a). Although both the Si and S isotopic ratios were measured in this grain, not enough information had been recorded to determine the S/Si and thus the $^{32}Si/^{28}Si$ ratio. Mixing lines are as described for the plot in the upper panel.

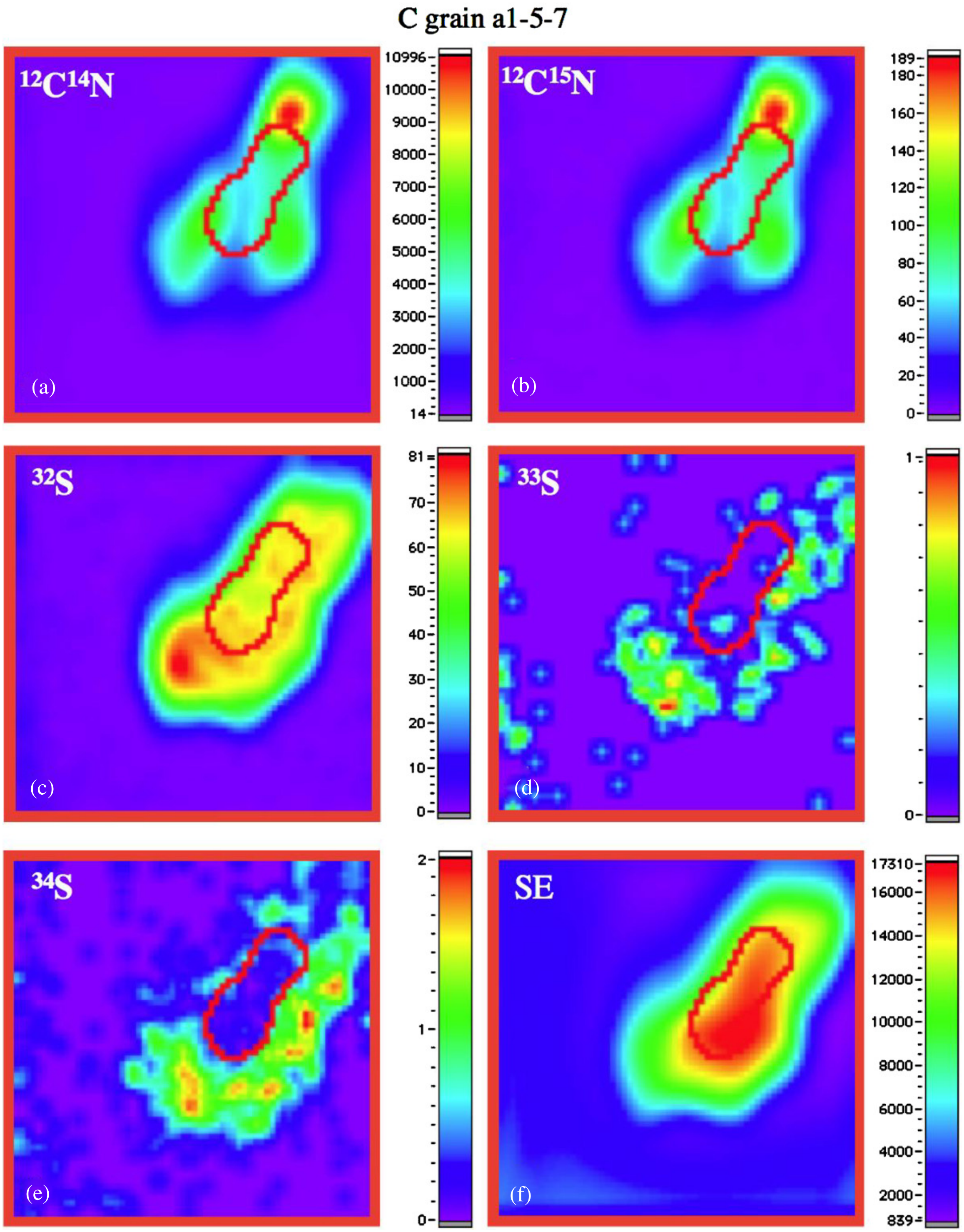

Figure 5. NanoSIMS images of CN and S negative ions and secondary electrons for the C grain a1–5–7. The images are over a 2.5 × 2.5 μm^2 area and consist of 64 × 64 pixels each. The color bars besides the images indicate counts pixel^{-1}. The area outlined by the red line was selected to exclude most contamination by ^{33}S and ^{34}S and was used to determine N and S isotopic ratios of the grain.

The inferred $^{26}Al/^{27}Al$ ratio ($\delta^{25}Mg/^{24}Mg = -172‰ \pm 167‰$, $\delta^{26}Mg/^{24}Mg = 2625‰ \pm 394‰$) of grain a1–5–7 is lower than those of other C grains, which in turn are lower than those of most X grains (Figure 2(a)). It is also lower than the mixing line of whole He/C (O/C + He/C) and He/N zones for the 12 $M_\odot$ and 15r SN models. However, mixing with the H envelope results in much lower $^{26}Al/^{27}Al$ ratios. Intermediate ratios can be produced by the proper mixing of all three zones. The C and Al isotopic ratios of grain a1–5–7 can be reproduced by a mixture of layer c in the 15r SN model with a 0.0063:0.9937 mix of a layer at internal mass 4.758 in the He/N zone and a layer at mass 4.87 in the H envelope (Figure 2(a)). They also can be reproduced by the same mixture of layers for the 15r4 SN model.

The mixing curves shown in Figures 1, 2(a), and 4 give only a very rudimentary impression of the mixing problem:

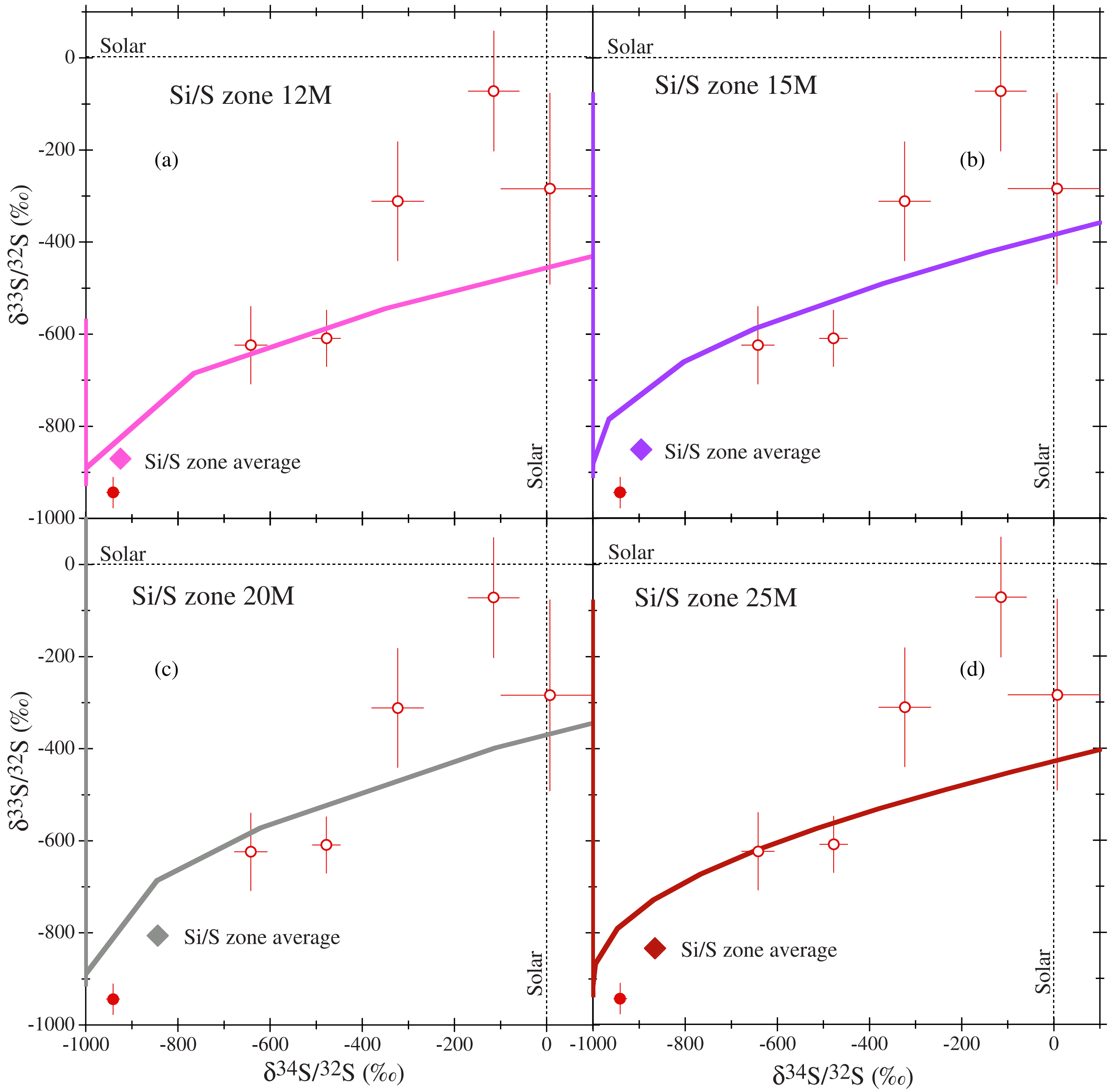

Figure 6. S isotopic ratios of C grains are compared to theoretical predictions of these ratios in the Si/S zones of four different SN models: the 12 $M_\odot$ SN model by Woosley & Heger (2007) and the 15 $M_\odot$, 20 $M_\odot$, and the 25 $M_\odot$ SN models by Rauscher et al. (2002). In addition to the ratio lines we also plotted the S isotopic ratios averaged over the Si/S zone for each model.

(1) they show only mixing curves for two isotopic ratios and (2) they usually involve only two or at most three different zones or layers. We thus attempted to match all isotopic ratios of a given grain by mixing several layers of the SN models we have considered. Table 2 shows the layers we have selected for this fitting exercise. The reasons for selecting these layers are the following. A layer in the core can provide a high abundance of ^{44}Ti without much affecting the other isotopic ratios. We chose a layer in the Si/S zone (12 $M_\odot$ model) and the C/Si zone (15r model) in order to obtain ^{28}Si for the X grains. In the He/C zone we selected two layers, one with high ^{29,30,32}Si/^{28}Si ratios and one with high ^{15}N. Both have high ^{12}C/^{13}C ratios. We need a layer in the He/N zone for high ^{26}Al/^{27}Al ratios, and finally one in the H envelope for low ^{26}Al/^{27}Al ratios and low ^{12}C/^{13}C ratios.

Table 3 and Figure 9 show the result of this fitting exercise for the C grain a1–5–7. The 12 $M_\odot$ SN model yields good fits for all measured isotopic ratios except the Si isotopic ratios. We remarked already in discussing Figure 4(a) that mixing lines of the 12 $M_\odot$ model do not reach grain a1–5–7. The 15r model can match the Si isotopic ratios and the ratios of the short-lived isotopes ^{26}Al, ^{32}Si, and ^{44}Ti of this grains quite well but has a problem with the C and N isotopic ratios. We have already seen in Figure 1 that the 15r model does not have a mixture that can reproduce the C and N isotopic ratios of grain a1–5–7. We thus produced two mixtures, one which matches the ^{12}C/^{13}C ratio of the grain but not the ^{14}N/^{15}N ratio and one which matches the N but not the C isotopic ratio. The first mixture matches all the remaining ratios, the second all but the ^{30}Si/^{28}Si ratio (Table 3 and Figure 9). The situation is similar for the 15r4 model except

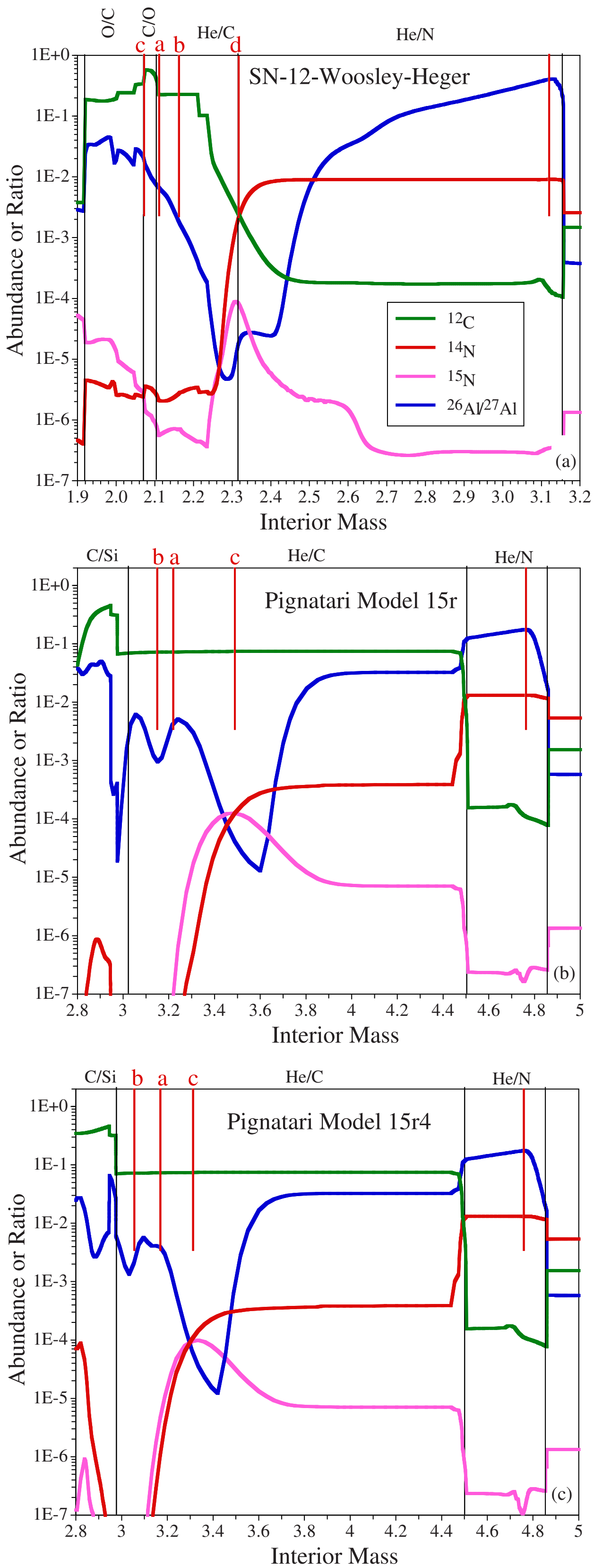

Figure 7. Carbon-12, ^{14}N, and ^{15}N abundances (weight fractions) and ^{26}Al/^{27}Al ratios in the interior of three SN models: (a) the 12 $M_{\odot}$ SN model by Woosley & Heger (2007) and ((b) and (c)) the 15r and 15r4 models by Pignatari et al. (2013c). Vertical lines across the height of individual plots indicate borders between SN zones named after the two most abundant elements (Meyer et al. 1995). Short vertical lines with labels indicate layers in the He/C zone that were mixed with the layer in the He/N zone indicated by another short vertical line. The interior mass (x-axis) is in units of solar mass.

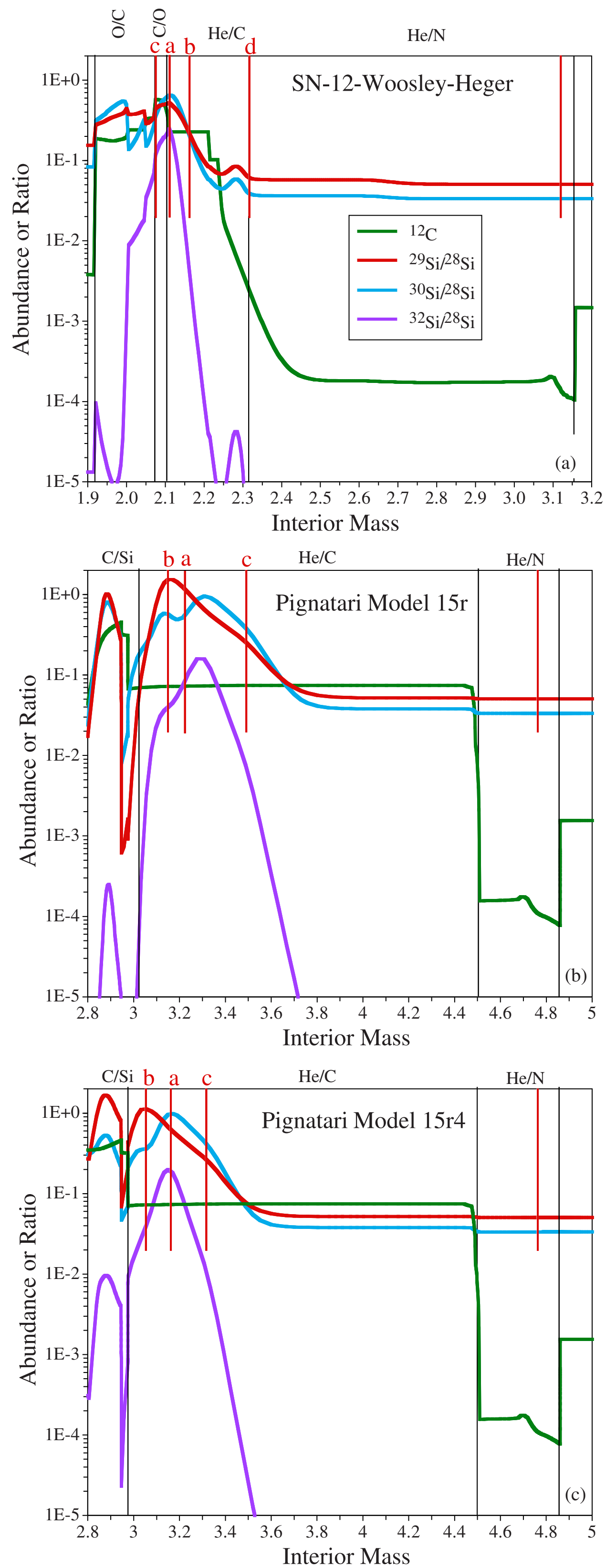

Figure 8. Carbon-12 abundances (weight fractions) and Si isotopic ratios in the interior of the two SN models described in the Figure 7 caption.

that the discrepancy for the ^{14}N/^{15}N ratio in case we match the ^{12}C/^{13}C ratio and vice versa is somewhat worse. We now obtain a closer match for the ^{30}Si/^{28}Si ratio in the second case (Figure 9 and Table 3).

Table 2
Isotopic Ratios in Different SN Layers Used for Fitting Grain Data

	$^{12}C/^{13}C$	C/O	$^{14}N/^{15}N$	$\delta^{29}Si/^{28}Si$ (‰)	$\delta^{30}Si/^{28}Si$ (‰)	$\delta^{33}S/^{32}S$ (‰)	$\delta^{34}S/^{32}S$ (‰)	$^{26}Al/^{27}Al$	$^{32}Si/^{28}Si$	$^{44}Ti/^{48}Ti$
12 M SN model[a]										
Core M 1.56	7.51E+1	1.52E−01	1.39E+0	−247	−921	15206	−785	4.85E+0	1.70E−7	3.36E+5
Si/S zone M 1.64	4.47E+2	6.95E−3	4.70E−2	−988	−999	−893	−999	1.83E−3	7.70E−9	9.24E+2
Si/S zone M 1.67	4.47E+2	6.95E−3	4.70E−2	−910	−752	−893	−999	1.83E−3	1.41E−8	9.24E+2
He/C zone M 2.110	9.82E+5	1.81E+1	4.05E+0	9049	17107	838	13721	6.99E−3	2.34E−1	2.86E−6
He/C–He/N border M 2.310	1.01E+6	7.55E−01	1.82E+1	223	144	869	16	1.26E−5	2.07E−6	1.65E−7
He/N zone M 3.125	3.38E+0	9.72E−01	2.83E+4	0	0	0	0	4.27E−1	7.43E−11	1.41E−9
H envelope M 3.185	1.84E+1	3.40E−01	2.09E+3	0	0	0	0	3.98E−4	0	0
15r SN model[a]										
Core M 1.682	3.02E+8	6.72E+2	3.85E+0	−961	3776	2534	26152	1.48E−6	3.01E−9	2.58E+5
C/Si zone M 2.946	5.87E+9	3.31E+0	1.02E+0	−988	−762	423	−537	4.55E−4	1.06E−10	2.56E+0
He/C zone M 3.214	1.01E+9	3.37E+0	3.72E−2	23385	14484	5688	59345	4.26E−3	7.47E−2	5.07E−4
He/C zone M 3.488	5.44E+5	6.88E+1	1.08E+0	4057	10500	3668	5018	4.31E−5	7.57E−3	1.19E−9
He/N zone M 4.758	3.90E+0	8.93E−1	8.34E+4	0	0	0	0	1.84E−1	0	0
H envelope M 4.87	1.89E+1	1.23E+1	4.36E+3	0	0	0	0	6.10E−4	0	0
15r4 SN model[a]										
Core M 1.897	1.40E+12	1.28E−1	2.01E−1	−1000	−1000	2531	26034	5.28E−2	8.92E−22	3.09E+6
He/C zone M 3.054	3.76E+9	5.59E+0	8.57E−1	20582	9032	5688	59345	2.10E−3	4.03E−2	1.01E−3
He/C zone M 3.307	1.28E+6	2.53E+0	1.17E+0	4347	11409	3668	5018	6.59E−5	1.34E−2	1.54E−9
He/N zone M 4.758	3.90E+0	8.94E−1	1.27E+5	0	0	0	0	1.76E−1	0	0
Envelope M 5.012	1.89E+1	2.90E−1	4.31E+3	0	0	0	0	5.80E−4	0	0

Note. [a] For each SN layer *M* indicates the mass coordinates in solar masses.

Table 3
Fit of Grain Isotopic Data to Supernova Models

Grain	$^{12}C/^{13}C$	$^{14}N/^{15}N$	$\delta^{29}Si/^{28}Si$ (‰)	$\delta^{30}Si/^{28}Si$ (‰)	$\delta^{33}S/^{32}S$ (‰)	$\delta^{34}S/^{32}S$ (‰)	$^{26}Al/^{27}Al$ (×1000)	$^{32}Si/^{28}Si$ (×1000)	$^{44}Ti/^{48}Ti$ (×1000)
C grain a1–5–7 data	192	58.4	1345	1272			1.70	4.54	42.2
12 M model	244	61.6	253	360			1.69	4.51	42.2
15r model match C	195	270	1507	1628			1.69	4.51	42.2
15r model match N	832	58.0	1284	2233			1.70	4.48	41.7
15r4 model match C	194	679	1629	463			1.69	4.53	41.1
15r4 model match N	1050	58.8	1357	1721			1.66	4.56	42.0
X grain a1–33–7 data	235	187	−683	−501	−47	−128	333		213
12 M model	236	186	−658	−528	−800	−918	222		212
15r model match C	233	516	−716	−456	362	−511	40.6		214
15r model match N	665	188	−744	−396	383	−518	49.8		218
X grain a2–28–7 data	693	124	−382	−553	−144	−72	119		118
12 M model	694	125	−535	−438	−675	−764	118		117
12 M model b[a]	696	124	−381	−553	−726	−820	117		120
15r model	695	125	−706	−312	388	−510	26.6		216

Note. [a] See text for explanation.

Table 4 shows the mixing fractions of the selected SN layers that give the best fit. As can be seen, the major contributions required are from the He/C zone and the H envelope, with only little contribution from the He/N zone, which lies between these zones. This addresses an issue that has been discussed before in connection with X grains: presolar grains from SNe appear to condense from mixtures of well-separated zones without including much material from zones in between. Recently, SN explosion models in multiple dimensions (e.g., Müller et al. 1991; Kifonidis et al. 2003; Joggerst et al. 2009; Hammer et al. 2010) have shown that during the explosion material from inner zones can penetrate into outer zones while overtaking intermediate zones. These models are still far from perfect, but isotopic data from SN presolar grains such as C grain a1–5–7 give evidence for these features during mixing.

3.2. X Grains and X-type Si_3N_4 Grains

The large ^{28}Si excesses in the X and Si_3N_4 grains of this study (Table 1 and Figure 3(a)) are comparable to those of previously studied X grains (e.g., Lin et al. 2010; Figure 10). Also their C and N isotopic ratios are typical of other X grains (Figure 1). An exception is the Si_3N_4 grain a1–3–2, which has extremely small C and N isotopic ratios ($^{12}C/^{13}C = 7.9$, $^{14}N/^{15}N = 4.5$) but Si isotopic ratios in the range of X grains ($\delta^{29}Si/^{28}Si = -434‰ \pm 6‰$, $\delta^{30}Si/^{28}Si = -317‰ \pm 6‰$; Figure 10). Although the C

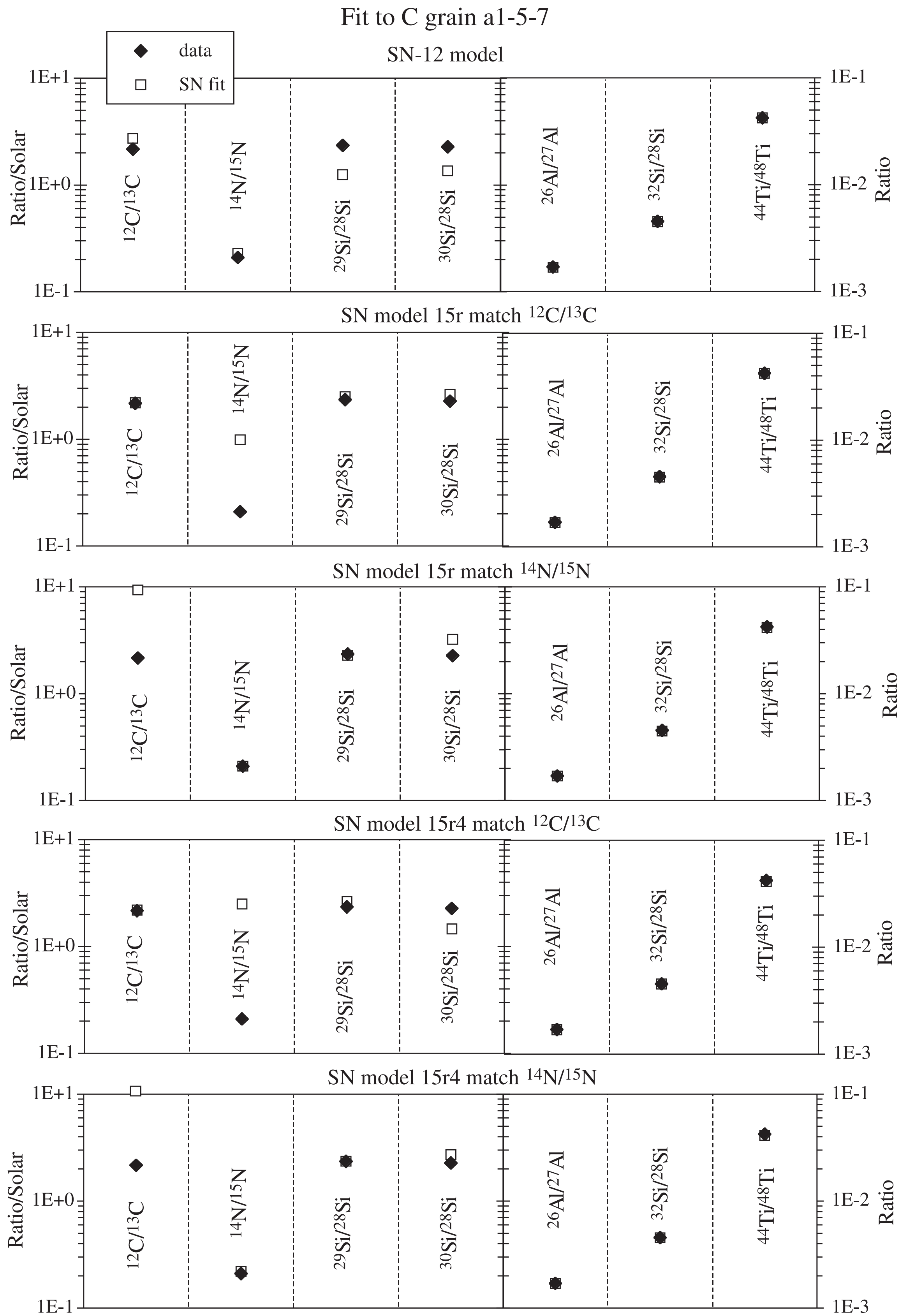

Figure 9. Results of fitting calculations of isotopic ratios of the C grain a1–5–7 to mixtures of contributions from different layers of three SN models: (a) the 12 $M_\odot$ SN model by Woosley & Heger (2007) and ((b) and (c)) the 15r and 15r4 models by Pignatari et al. (2013c). Plotted are the isotopic ratios measured in the grain and the ratios calculated for the mixture. For stable isotopes the ratios are normalized to the solar system ratios (left-hand scale), for the short-lived isotopes ^{26}Al, ^{32}Si, and ^{44}Ti the ratios are plotted (right-hand scale). Two fitting results are presented for the 15r and 15r4 models, one that matches the ^{12}C/^{13}C ratio, and one that matches the ^{14}N/^{15}N ratio of the grain.

Table 4
Mixing Fractions of Different SN Layers

	C-grain a1–5–7		X-grain a1–33–7		X-grain a2–28–7	
12 M SN model[a]						Fit b[b]
Core M 1.56	0.02		0.04		0.02	0.02
Si/S zone M 1.64 and 1.67[c]			1.09		0.41	0.56
He/C zone M 2.11	3.66		2.12		9.10	9.10
He/C zone M 2.16	0.34					
He/C–He/N border M 2.31	39.41		36.28		35.90	35.94
He/N zone M 3.125	0.28		54.43		26.33	26.35
H envelope M 3.185	56.30		6.05		28.24	28.03
15r SN model[a]	Match C[d]	Match N[e]	Match C[d]	Match N[e]		
Core M 1.682	0.04	0.01	0.10	0.00		
C/Si zone M 2.946		0.33	1.79	3.05	2.84	
He/C zone M 3.214	2.70	3.31				
He/C zone M 3.488	13.52	42.98	9.89	25.91	30.95	
He/N zone M 4.758	0.50	0.48	21.39	25.30	12.90	
H envelope M 4.87	83.23	52.90	66.83	45.73	53.31	
15r4 SN model[a]	Match C[d]	Match N[e]				
Core M 1.897	0.39	0.23				
He/C zone M 3.054	9.99	3.76				
He/C zone M 3.307	6.33	49.22				
He/N zone M 4.758	0.46	0.46				
Envelope M 5.012	82.83	46.32				

Notes. Given are the fractions in percent of each SN layer to reproduce the isotopic compositions of three grains. The fits are given in Table 2.
[a] For each SN layer M indicates the mass coordinates in solar masses.
[b] See text for explanation.
[c] $M = 1.64$ for grain 2–28–7 and $M = 1.67$ for grain 1–33–7.
[d] Mixture that best matches the $^{12}C/^{13}C$ ratio of the grain.
[e] Mixture that best matches the $^{14}N/^{15}N$ ratio of the grain.

and N isotopic ratios of this grain are comparable to those of nova candidates, an SN origin is more likely than a nova origin. Nittler & Hoppe (2005) found a SiC grain with similar C, N, and Si isotopic ratios, but measured a large ^{49}Ti excess and proposed that it has an SN origin. Unfortunately, our grain was consumed during the S and N imaging analysis, and no material was left for Mg–Al and Ca–Ti measurements. Its S isotopic ratios are normal within large errors ($\delta^{33}S/^{32}S = -83‰ \pm 121‰$ and $\delta^{34}S/^{32}S = -67‰ \pm 51‰$).

As seen in Table 1 and Figure 3(b), Type X grains tend to have ^{32}S excesses. The weighted means of the S isotopic ratios are $\delta^{33}S/^{32}S = -64‰ \pm 22‰$ and $\delta^{34}S/^{32}S = -53‰ \pm 8‰$ (1σ errors). Errors of individual grain measurements however are large, and many grains have normal S isotopic ratios within 2σ errors. Only three grains (a2–10–3, a2–28–7, and a2–45–9) have ^{33}S and ^{34}S deficits of more than 2σ, whereas another six grains (a1–20–7, a1–22–4, a1–37–7, a1–42–3, a1–48–1, and a2–14–8) have either ^{33}S or ^{34}S deficits of more than 2σ. Excesses in ^{33}S and/or ^{34}S in some grains are all smaller than 2σ. In Figure 3(c), we show correlation plots between the $\delta^{34}S/^{32}S$ and $\delta^{30}Si/^{28}Si$ values for all of our X grains and for previously reported grains. It is generally accepted that X grains come from SNe because only massive stars produce large ^{28}Si excesses. In conventional core–collapse SN models (e.g., Rauscher et al. 2002), ^{28}Si is produced by oxygen burning, and the resulting Si/S zone is also rich in ^{32}S. In Figure 3(c) we plotted a mixing line of material from the Si/S zone with a He/C–He/N mix of the 15 $M_\odot$ SN model by Rauscher et al. (2002). It is clear that, except for one X grain, all other data points for X grains plot above this line, indicating that ^{32}S excesses (^{34}S deficits) are much smaller than

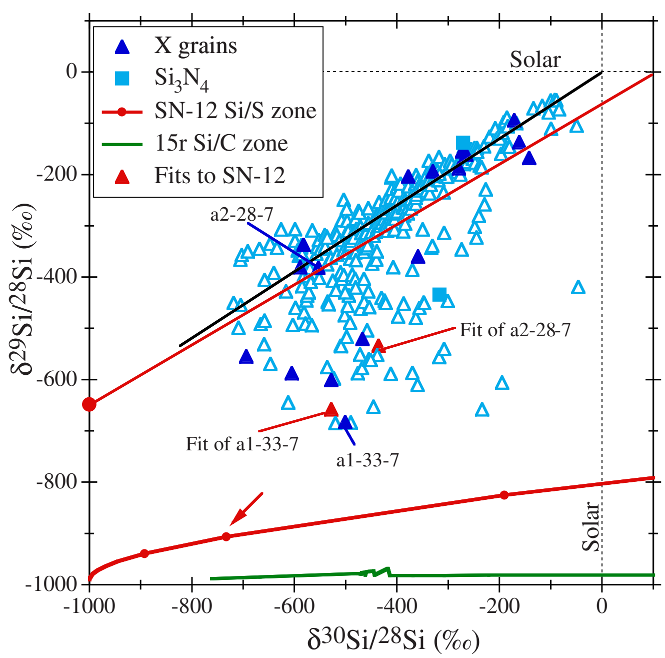

Figure 10. Three-isotope plot of the Si isotopic ratios of X grains and Si_3N_4 grains. The two lines at the bottom of the plot are the Si isotopic ratios in the Si/S zone of the 12 $M_\odot$ SN model and in the C/Si zone of the 15r model. The isotopic ratios of two selected X grains and the ratios obtained by fitting all measured isotopic ratios except S to mixtures of layers of the 12 $M_\odot$ SN model are indicated. The solid circle on the y-axis is the proposed ratio of the Si/S zone that would give a perfect fit for the Si isotopic ratios of grain a2–28–7. The line through this composition and that of the grain extrapolates to $\delta^{29}Si = 163‰$, $\delta^{30}Si = 200‰$, the composition of the other layers in the mix.

expected for such a mix. The most likely explanations are low intrinsic S concentrations and contamination with isotopically normal S. We will address this problem in detail below.

In the model by Pignatari et al. (2013b), ^{28}Si is produced in explosive He-burning conditions by a chain of α-captures starting from ^{16}O at the bottom of the He/C zone during passage of the shock wave. These authors proposed that X grains formed from this C/Si zone. The α-captures also produce other α-nuclei including ^{32}S. In Figure 3(c) we plot the average δ^{34}S/^{32}S and δ^{30}Si/^{28}Si values in the C/Si zone of model 15r. Whereas these values can explain the δ^{34}S/^{32}S and δ^{30}Si/^{28}Si values of most X grains if we allow for contamination, the lowest δ^{30}Si/^{28}Si value of the model is not quite as low as the values of some X grains. More importantly, the average δ^{33}S/^{32}S value of the C/Si zone is +650‰, in contrast to ^{33}S depletions in many X grains (Figure 3(b)) and for the average of X grains. Due to this discrepancy, the S isotopic ratios in X grains seem to argue against this model as a source of X grains. On the other hand, the Pignatari et al. (2013b) model avoids the problem of the lack of ^{54}Fe excesses in X grain (Marhas et al. 2008), which are expected for the Si/S zone of conventional SN models such as those by Rauscher et al. (2002). The Pignatari et al. (2013b) model has not yet been explored in all details. Here we restrict ourselves to the isotopic ratios of a few elements with an emphasis on S, but in the future will compare the isotopic ratios of other elements such as Ti, Fe, and Ni with the model.

The N, Al, and Si isotopic ratios of X grains and the problems of matching them with SN models have been discussed before (e.g., Besmehn & Hoppe 2003; Lin et al. 2010). Here we return to these problems by considering two SN models that have not been considered before. Figure 1 compares the N and C isotopic ratios of X grains and the two Si_3N_4 grains of this study with predictions of mixtures for the 12 $M_\odot$ core–collapse SN model by Woosley & Heger (2007) and the 15r model by Pignatari et al. (2013b, 2013c). As has been mentioned before, mixtures of whole zones do not come close to explaining the isotopic ratios of essentially all the grains and for the 15r model the mixture of the mass 3.488 $M_\odot$ layer (layer c in Figures 7(b) and 8(b)) with a layer in the H envelope, which yields the lowest ^{14}N/^{15}N ratios, misses most of the grains. The situation is more promising for mixtures involving the mass 2.31 $M_\odot$ layer of the 12 $M_\odot$ SN model (layer d in Figures 7(a) and 8(a)), which can cover most of the grains. A recent analysis of ^{15}N production in the He shell during the SN explosion (Meyer & Bojazi 2011; Bojazi & Meyer 2014) shows that the use of an updated set of nuclear reaction rates reduces by a factor of four the amount of ^{15}N made in the He/C zone compared to previous calculations (e.g., Rauscher et al. 2002). Considering the nuclear reaction rates affecting the production of ^{15}N in the He shell (see Bojazi & Meyer 2014), the 12 $M_\odot$ SN model considered here was calculated by using a network mostly consistent with that of Rauscher et al. (2002; e.g., Woosley et al. 2004). The set of nuclear reaction rates adopted to calculate the 15r model is given by Pignatari et al. (2013a), and did not include the set of reaction rates by Iliadis et al. (2010). Therefore, the ^{15}N peak obtained at 2.31 $M_\odot$ in the 12 $M_\odot$ SN model (layer d) and at 3.488 $M_\odot$ in the 15r model (layer c) could be affected by the reaction rates adopted, making it even more challenging to explain low ^{14}N/^{15}N ratio together the low ^{12}C/^{13}C ratio. In any case, without considering potential nuclear uncertainties, mixing with layer d layer in the 12 $M_\odot$ SN model (Figure 1) achieves lower ^{14}N/^{15}N ratios than any previous mixing not involving the ^{15}N spike in the He/N zone (see Figure 17 in Lin et al. 2010).

Figure 2 shows the inferred initial ^{26}Al/^{27}Al and ^{44}Ti/^{48}Ti of the X grains of this study and of previously analyzed X grains (Lin et al. 2010). Many grains in the ^{26}Al/^{27}Al versus ^{12}C/^{13}C plot lie above mixing lines between the He/C and He/N zones. That SN models cannot produce ^{26}Al/^{27}Al ratios as high as those observed in some X grains and low-density graphite grains (Jadhav et al. 2013) has been discussed before (Lin et al. 2010) and still awaits a solution. On the other hand, as discussed in connection with the C grain a1–5–7, intermediate ^{26}Al/^{27}Al ratios can be produced by mixing with the H envelope. TiC subgrains have been found in the transmission electron microscope in mainstream SiC grains (Bernatowicz et al. 1992) and possibly in an X grains (Hynes et al. 2010). In X grains, Ti is concentrated in small subgrains as evidenced by depth profiles during isotopic analysis (Lin et al. 2010) and by ion imaging (Zinner et al. 2011). An important question is whether these subgrains condensed before SiC formation or whether they are the result of exsolution of Ti that condensed into SiC as solid solution. Titanium isotopic heterogeneity among different subgrains within a given X grain would indicate the former. The X grains of this study are too small to address this question, but we hope that isotopic analysis of large X grains will provide an answer.

As we did for the C grain a1–5–7, we performed detailed fitting calculations of mixtures from our two SN models to all isotopic ratios measured in two selected X grains. In contrast to the C grain a1–5–7, we performed the fitting calculations on these two X grains only for model 15r and not for model 15r4. The reason is that only model 15r produces ^{28}Si excesses in the C/Si zone, whereas model 15r4 does not. Throughout the C/Si zone there are ^{29}Si and ^{30}Si excesses in the 15r4 model. The smallest $\delta^{29,30}$Si values in this zone are δ^{29}Si = +251‰ and δ^{30}Si = +404‰. The selected grains both had their ^{44}Ti/^{48}Ti ratios determined and they have different Si isotopic ratios. One, grain a2–28–7, plots close to the correlation line (solid black line) along which most X grains plot in a Si 3-isotope diagram (Figure 10). Grain a1–33–7, in contrast, is the grain that plots farthest away from this line among the X grains of the present study. Shown in Figure 10 are also the Si isotopic compositions of different layers of the Si/S zone of the 12 $M_\odot$ SN model by Woosley & Heger (2007) and the C/Si zone of the 15r model by Pignatari et al. (2013b, 2013c). These are the most ^{28}Si-rich layers in these two models. In order to match the Si isotopic ratios of grain a1–33–7 we use the layer at 1.67 internal mass of the 12 $M_\odot$ SN model (indicated by an arrow in Figure 10). A proper mixture of this layer with the mixture of all the other layers (having δ^{29}Si = 163‰, δ^{30}Si = 200‰) yields a composition quite close to the original position. The results of the fit for all isotopic ratios are shown in Figure 11 and Table 3, with mixing fractions given in Table 4. The ^{26}Al/^{27}Al ratio of the grain is a little too high to be fitted by the 12 $M_\odot$ SN model. We have not tried to fit the measured S isotopic ratios of this grain but in Figure 11 have plotted the ratios of the mixture that gives a close fit to the Si isotopic ratios. The fit to layers of the 15r model works almost equally well for the Si isotopic ratios, but here we encounter the same problem as for the C grain a1–5–7: either we can achieve a close match for the C isotopic ratio or for the N isotopic ratio, but not for both of them (Figure 11 and Table 3). Furthermore, we cannot match the ^{26}Al/^{27}Al ratio of the grain: the 15r model does not achieve as high ^{26}Al/^{27}Al ratios as the 12 $M_\odot$ model in the He/N zone (Figures 2(a) and 7). Both models can achieve a perfect fit for the ^{44}Ti/^{48}Ti ratio. In order to achieve such a fit for the case of the match to the ^{12}C/^{13}C in the 15r model we need a small

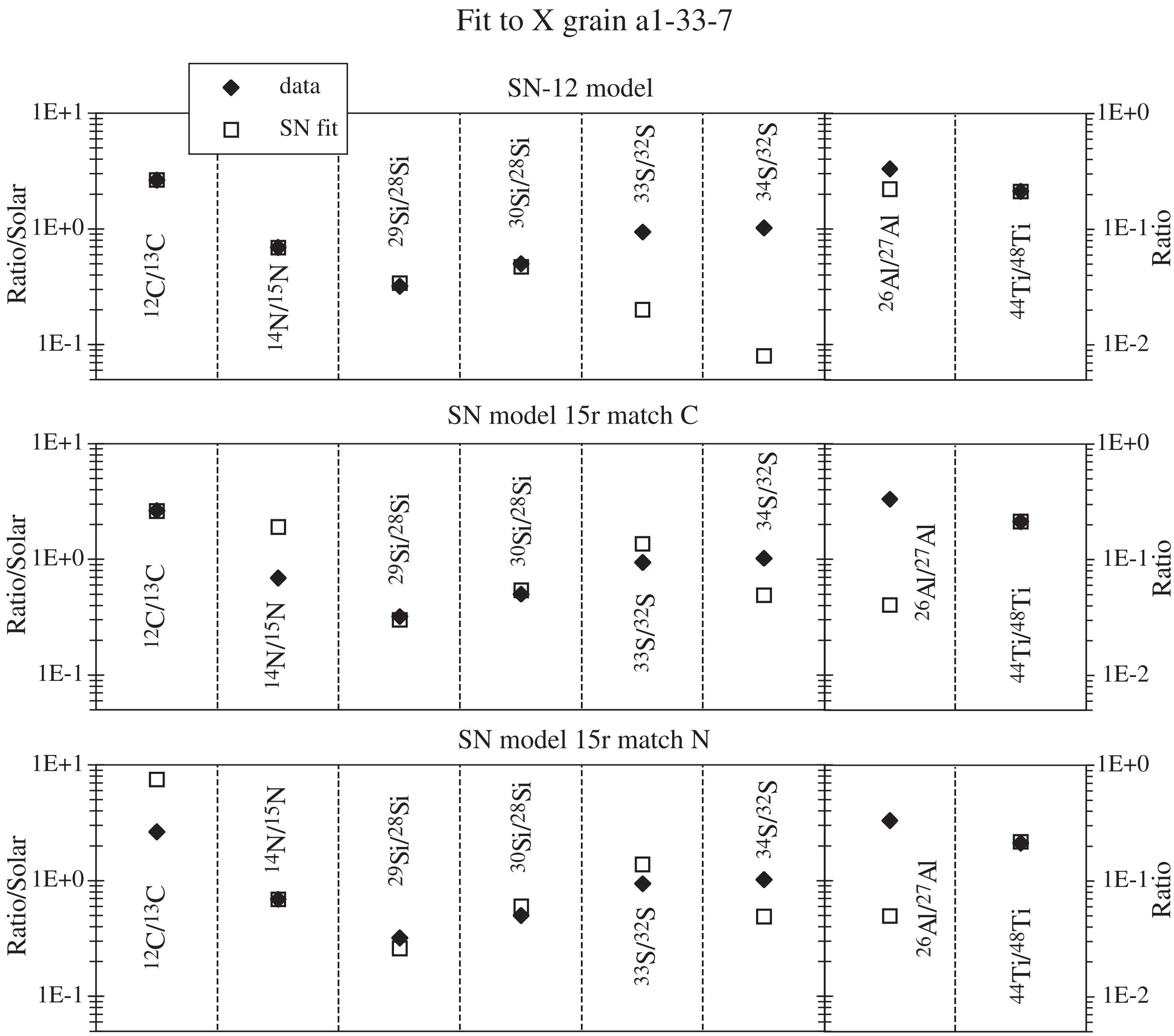

Figure 11. Results of fitting calculations of isotopic ratios of the X grain a1–33–7 to mixtures of contributions from different layers of the two SN models considered. The convention is the same as for Figure 9. For the 15r model two fitting results are presented, one that matches the $^{12}C/^{13}C$ ratio and one that matches the $^{14}N/^{15}N$ ratio of the grain.

contribution from the core (Table 4), whereas for the other cases the ^{44}Ti contribution from the C/Si zone is sufficient. This is in contrast to the claim by Pignatari et al. (2013b) that no contribution from the core is necessary. However, we need to point out that grain a1–33–7 has the second-highest $^{44}Ti/^{48}Ti$ ratio (Figure 2) and it is possible that none of the X grains with smaller $^{44}Ti/^{48}Ti$ ratios need any contributions from the core. Furthermore, the Pignatari et al. (2013b) models were calculated for only one stellar mass. At the moment we do not know whether or not models with a lower initial mass (e.g., a 12 $M_\odot$ star) would fit the grain data, but it is our goal to investigate a range of initial masses in the future. Figure 1 shows that we can match the C and N isotopic ratios with a mix between layer c and the H envelope, but such a mixture gives a complete mismatch for the Al and Si isotopic ratios.

From Figure 10 it is clear that the Si isotopic ratios of grain a2–28–7 cannot be matched if we use any compositions of the SN models in a mix with the rest of the layers (that have δ^{29}Si = 513‰, δ^{30}Si = 862‰ for the 12 $M_\odot$ model). The best match achieved with the layer at internal mass 1.64 of the 12 $M_\odot$ model (that has a composition closest to the origin of the Si plot in Figure 10) lies on the mixing line between these compositions with the closest distance to the measured data point (Figures 10 and 12 and Table 3). As has been discussed before (Lin et al. 2010), in order to achieve a match for grain a2–28–7 and most X grains along the major correlation line one needs a component with a much higher ^{29}Si abundance. As an exercise we increased the ^{29}Si abundance of the layer at internal mass 1.64 from 2.57×10^{-4} to 7.40×10^{-3} and achieved a perfect fit (model (b) in Figure 12 and Table 3). For the 15r model we have not tried an artificial increase in the ^{29}Si abundance in the C/Si zone. However, the model does not match the $^{26}Al/^{27}Al$ ratio of the grain and produces too much ^{44}Ti.

On the face of it, the 15r model comes closer to the measured S isotopic ratios. However, as already mentioned, it predicts ^{33}S excesses, whereas, on average, the X grains have ^{33}S deficits.

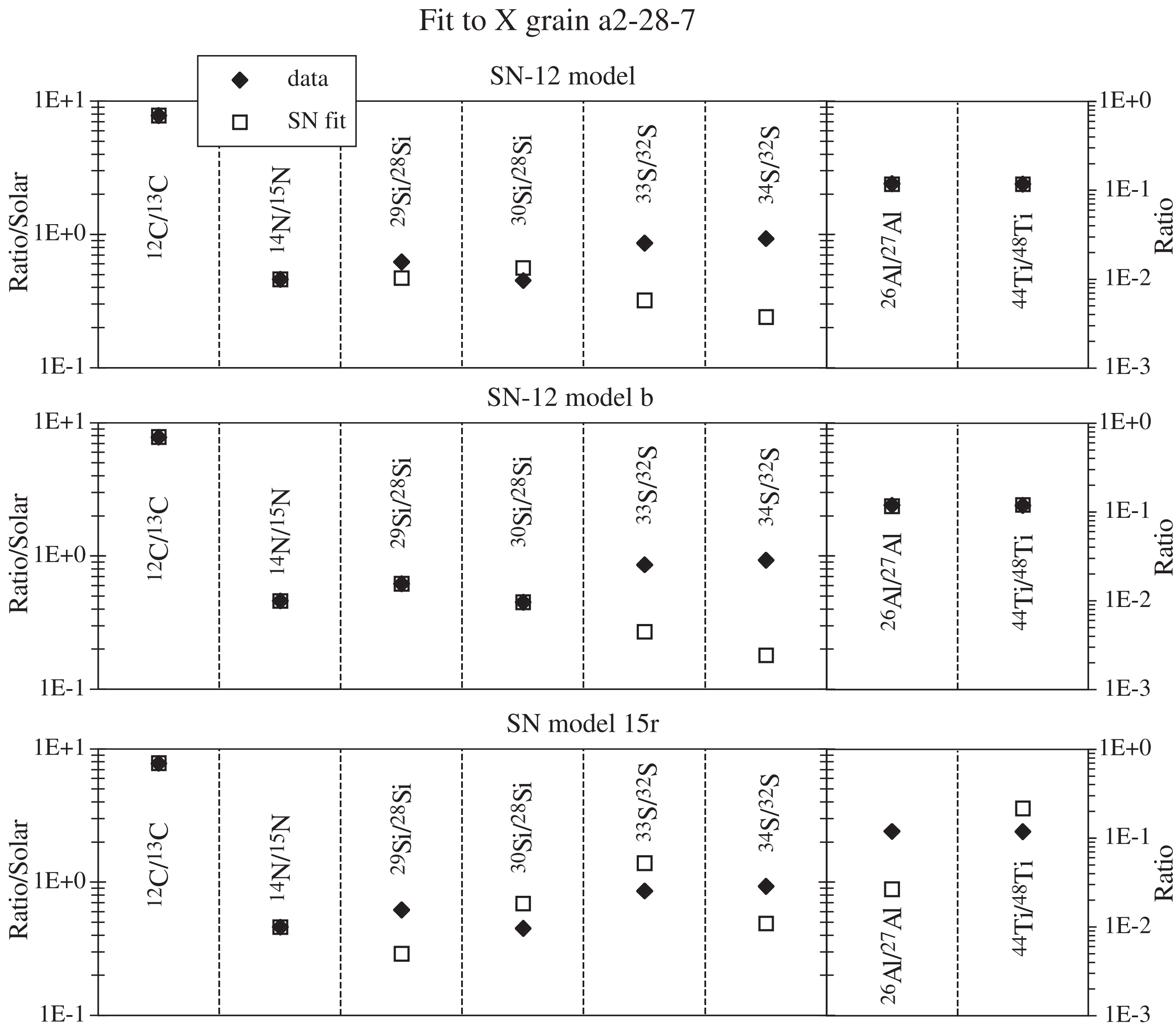

Figure 12. Results of fitting calculations of isotopic ratios of the X grain a2–28–7 to mixtures of contributions from different layers of the two SN models considered. The convention is the same as for Figure 9. In case (b) of the 12 $M_\odot$ SN model we artificially increased the ^{29}Si abundance in the Si/S zone in order to match the Si isotopic ratios of the grain.

The most likely explanation for the mismatch between the measured S isotopic compositions and the much larger ^{33,34}S deficits predicted by the 12 $M_\odot$ SN model is contamination by terrestrial S, most likely introduced by the treatment with sulfuric acid during grain processing. In the previous discussion of C grains we pointed out that only very little S condenses into SiC grains. On average, X grains have even lower abundances of incompatible trace elements than other types of presolar SiC grains (Amari et al. 1995; Henkel et al. 2007). Figure 5 also clearly shows how much of a role contamination plays for the C grain.

We have determined the S/Si atomic ratios for all grains of this study in the same way as we described it for the C grain. They are given in Table 1 and Figure 13. The S in C grain a1–5–7 (upper point in Figure 13) is completely dominated by the radiogenic ^{32}S. If we assume that the ^{33}S and ^{34}S measured in the image of this grain is from contamination with isotopically normal S, we can calculate the concentration of this S and obtain the lower point in the plot. As already argued in the previous section, the original intrinsic S of this grain must be even lower because the models predict excesses in ^{33}S and ^{34}S in the layers with ^{32}Si and thus the intrinsic ^{32}S would be even lower than in the case that the non-radiogenic S in the measurement has normal isotopic composition. It can be seen in Figure 13 that the S abundances in all other grains are larger than what we consider the intrinsic and/or contamination S abundance in the C grain, in some cases by a large factor. It is thus very likely that the S in these other grains is dominated by contamination.

Because the S isotopic anomalies in the X grains are much smaller than in the C grain, contamination is more difficult to detect in the S ion images of the X grains. In grain a1–33–7 (Figure 14) the ion images of CN and of S are not aligned with the secondary electron image. The overall image is isotopically normal in S with δ^{33}S = 40‰ ± 36‰, δ^{34}S = 0‰ ± 15‰. Two spots with high S concentrations are located at the edges of the grain and are most likely contamination. Both are isotopically

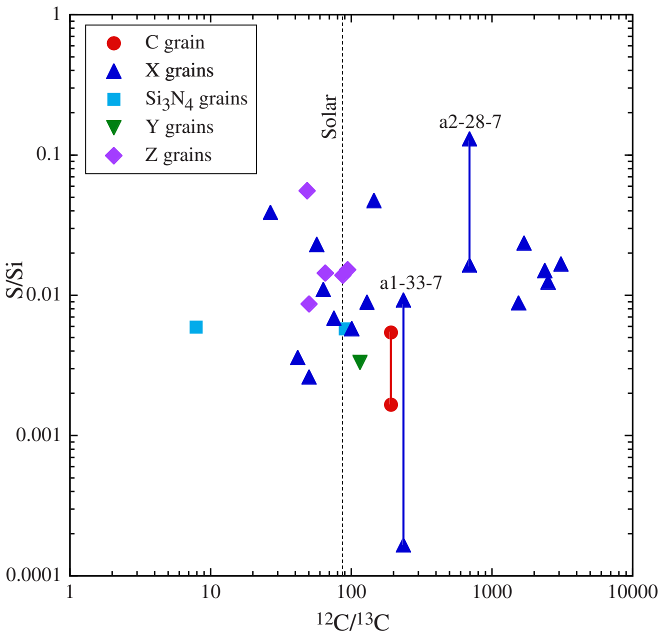

Figure 13. Atomic S/Si ratios of the grains of this study are plotted against their C isotopic ratios. The lower point for the C grain is the S abundance for contamination assumed to have normal S isotopic ratios. For the two X grains a1–33–7 and a2–28–7 the lower points are the amounts of S calculated to have the S isotopic composition predicted by the fit to the Si isotopic ratios if the rest of the S is isotopically normal contamination.

normal: the left spot has $\delta^{33}S = -14‰ \pm 69‰$, $\delta^{34}S = 5‰ \pm 29‰$ and the right spot $\delta^{33}S = 44‰ \pm 75‰$, $\delta^{34}S = -28‰ \pm 31‰$. However, we found three areas with anomalies in ^{34}S. These areas are indicated by the two circles and the ellipse in Figure 14. Their combined δ-values are $\delta^{33}S = -47‰ \pm 107‰$, $\delta^{34}S = -128‰ \pm 43‰$ (spot 1: $\delta^{33}S = 251‰ \pm 280‰$, $\delta^{34}S = -156‰ \pm 96‰$; spot 2: $\delta^{33}S = -252‰ \pm 200‰$, $\delta^{34}S = -101‰ \pm 92‰$; spot 3: $\delta^{33}S = -66‰ \pm 138‰$, $\delta^{34}S = -129‰ \pm 56‰$). Of course, the question arises whether these anomalies can be the result of statistical fluctuations. The data do not support this possibility. The total area of the three spots is about 5% of the total area of the grain indicated by the secondary electron image (Figure 14(f)) and the total ^{32}S count in these spots is about 9% of the ^{32}S count in the whole image. The anomaly in ^{34}S is 3σ, which would happen in only 0.4% of the cases if it is the result of statistical fluctuations. We thus give this S isotopic composition as that of the grain in Table 1. This still falls short of the S δ-values predicted by the fitting to the 12 $M_\odot$ model (Table 3 and Figure 11). If we explain this difference by contamination with isotopically normal S, we would have to add 6.2 times as much isotopically normal S to S with the isotopic composition predicted by the fitting from the Si isotopic ratios to obtain $\delta^{33}S = -111‰$, $\delta^{34}S = -128‰$. Since the isotopically anomalous region has only 9% of the total S, the S/Si ratio of the S with the predicted S isotopic composition would be only 1.8% of the total (lower point in Figure 13).

Grain a2–28–7 is different in that the whole grain has an anomalous S isotopic composition with $\delta^{33}S = -118‰ \pm 23‰$, $\delta^{34}S = -54‰ \pm 10‰$. Table 1 gives a somewhat more anomalous composition of a sub-region ($\delta^{33}S = -144‰ \pm 39‰$, $\delta^{34}S = -72‰ \pm 17‰$), which, however, agrees with that of the whole grain within errors. Here again, we can calculate how much isotopically normal S do we have to add to a grain with the δ-values $\delta^{33}S = -675‰$, $\delta^{34}S = -764‰$ predicted from the fit to the 12 $M_\odot$ SN model (Table 3) in order to obtained the measured overall composition. Sulfur of the predicted composition mixed with about 3.7 times as much isotopically normal S results in a composition of $\delta^{33}S = -144‰$, $\delta^{34}S = -163‰$, agreeing with the measured $\delta^{33}S$ value, but not the $\delta^{34}S$ value. To achieve agreement with the $\delta^{34}S$ value we have to add 9.5 as much isotopically normal S. Figure 13 shows the amount of S in the putative original grain as the lower symbol of grain a2–28–7 if we add an average of five times as much normal S.

To demonstrate the difficulties faced in such measurements, we show isotopic images of three more X grains. In grain a1–22–4 (Figure 15), the CN signal is well aligned with the secondary electron signal and the $^{14}N/^{15}N$ ratios is uniform across the grain. Most of the S signal comes from a strip along the left edge of the grain and is isotopically normal ($\delta^{33}S = 3‰ \pm 32‰$ $\delta^{34}S = -23‰ \pm 14‰$). On the other hand, the area within the circle, centered on the CN and secondary electron images, has anomalous S ($\delta^{33}S = -87‰ \pm 61‰$, $\delta^{34}S = -56‰ \pm 24‰$). Again, there is strong circumstantial evidence that the S is dominated by contamination with terrestrial S.

Grain a1–48–1 is another grain with complex isotopic images (Figure 16). Although the $^{12}C^{15}N$ signal is highest at the edges, the $^{14}N/^{15}N$ ratio is uniform over the main grain at the value 107. However, there is a small grain located above the main grain, easily recognized by the $^{12}C^{14}N$ hotspot in Figure 16(a). This grain has $^{14}N/^{15}N = 1197$, typical of mainstream grains. We do not know what fraction of the Si signal came from this attached grain. Although it must have been small, the $\delta^{29,30}Si$ values of grain a1–48–1 given in Table 1 must be considered upper limits. Most of the S signal comes from a ring around the main grain and it is isotopically normal within 2σ ($\delta^{33}S = 115‰ \pm 60‰$, $\delta^{34}S = 5‰ \pm 23‰$). In contrast, the area within the circle has a ^{34}S deficit ($\delta^{33}S = 182‰ \pm 159‰$, $\delta^{34}S = -124‰ \pm 57‰$).

Finally, grain a2–45–9 is also complex. It consists of a main grain on the left and a smaller grain on the right (Figure 17). The separation is clearly seen in the $^{12}C^{15}N$ image (Figure 17(b)). The main grain is the X grain with a $^{14}N/^{15}N$ ratio of 73, whereas the grain on the right has $^{14}N/^{15}N = 1369$ and is most likely a mainstream grain. Again, because of the presence of the second grain, the $\delta^{29,30}Si$ values of this grain in Table 1 must be considered upper limits. Most of the S signal comes from the lower edge of the grain and is isotopically normal. The area within the circle on the left is anomalous in S with $\delta^{33}S = -249‰ \pm 109‰$, $\delta^{34}S = -120‰ \pm 49‰$. Interestingly, the area within the circle on the right is also anomalous ($\delta^{33}S = -98‰ \pm 100‰$, $\delta^{34}S = -74‰ \pm 42‰$), but not outside of 2σ.

In summary, isotopic images are complex. In many cases, S signals appear to come from the edges of the grains, indicating contamination. These areas are almost always isotopically normal. Isotopic anomalies are found in areas with lower S ion signals but are still smaller than those expected on the basis of the Si isotopic ratios (Figure 3(c) and Table 3). Although we cannot directly proof it, we believe that contamination with terrestrial S is the most likely explanation of this discrepancy.

3.3. One Y Grain and Five Z Grains

Only one Y grain and five Z grains were selected for N and S isotopic analysis. The Y grain has an extremely large ^{30}Si excess ($\delta^{29}Si/^{28}Si = -154‰ \pm 7‰$, $\delta^{30}Si/^{28}Si = 874‰ \pm 16‰$) and all five Z grains have ^{30}Si excesses larger than those of most other Z grains (see data base; Hynes & Gyngard 2009).

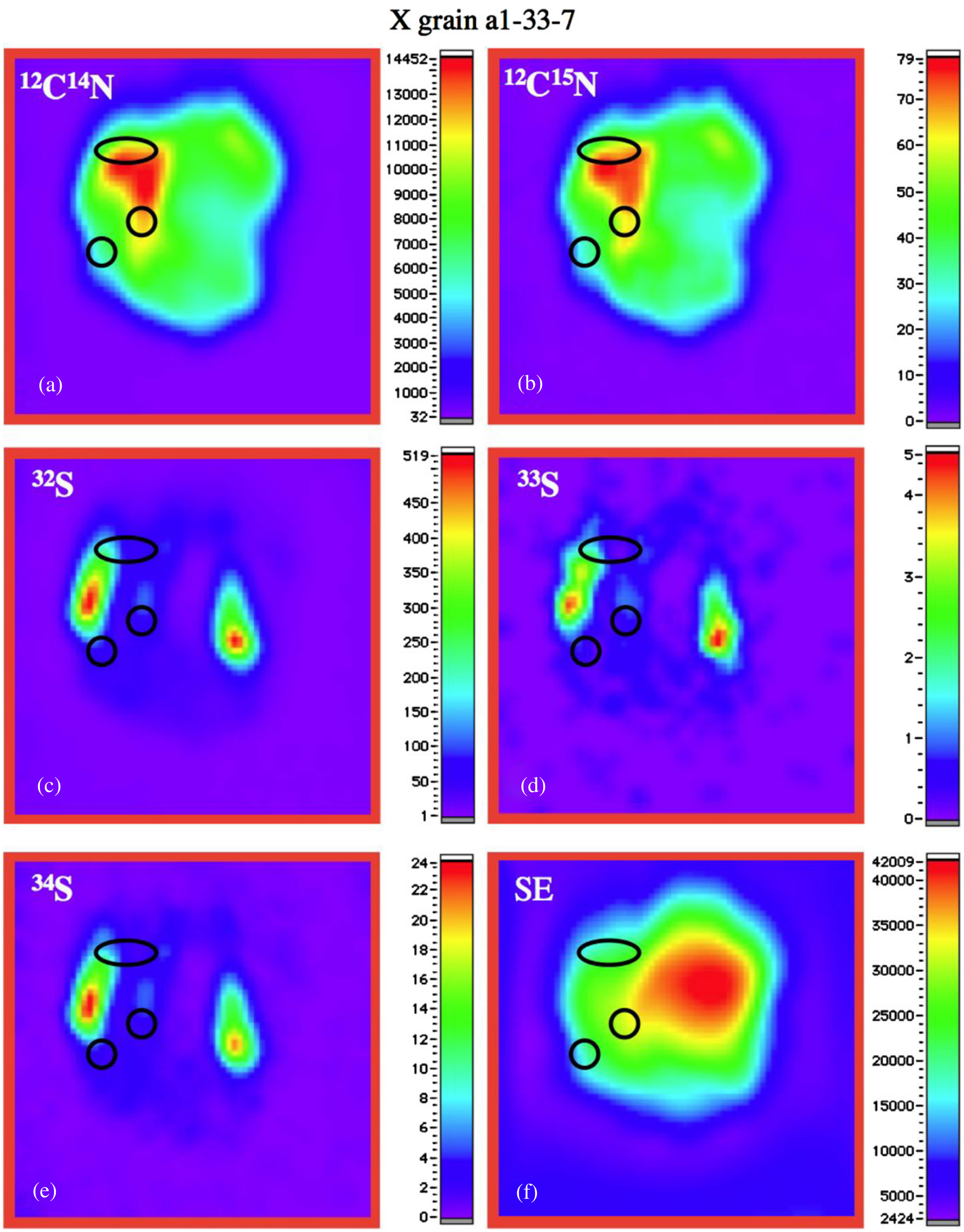

Figure 14. NanoSIMS images of CN and S negative ions and secondary electrons for the X grain a1–33–7. The images are over a 2.5 × 2.5 μm^2 area and consist of 64 × 64 pixels each. In this and the next three figures, the color bars besides the images indicate counts $pixel^{-1}$. The two black circles and the ellipse indicate areas isotopically anomalous in S. In contrast, the two areas with the strongest S signals are isotopically normal.

Presolar SiC grains of type Y and Z are thought to originate from low-mass AGB stars of 1/2 and 1/3 solar metallicity, respectively (Amari et al. 2001; Zinner et al. 2006); however, the Z grains of this study must have come from stars of even lower metallicity. In Figure 18(a) we plot lines depicting the evolution of the Si isotopic ratios in AGB stars of 2 $M_{\odot}$ and 3 $M_{\odot}$ and metallicity $Z = 0.003$, ∼1/6 of solar metallicity, and $Z = 0.002$, 1/10 of solar metallicity. The AGB models we use are the Torino models described in detail by Gallino et al. (1998) and Bisterzo et al. (2010). For predictions of the Si isotopic ratios we use the cross sections of Guber et al. (2003), which, as has been shown by Zinner et al. (2006), describe the Si isotopic ratios of Y and Z grains better than those of Bao et al. (2000). As can be seen, the 2 $M_{\odot}$ models do not reach the large $\delta^{30}Si/^{28}Si$ values of our grains. Whereas almost all Z grains lie above the $M = 3\,M_{\odot}$ and $Z = 0.003$ line (Zinner et al. 2006),

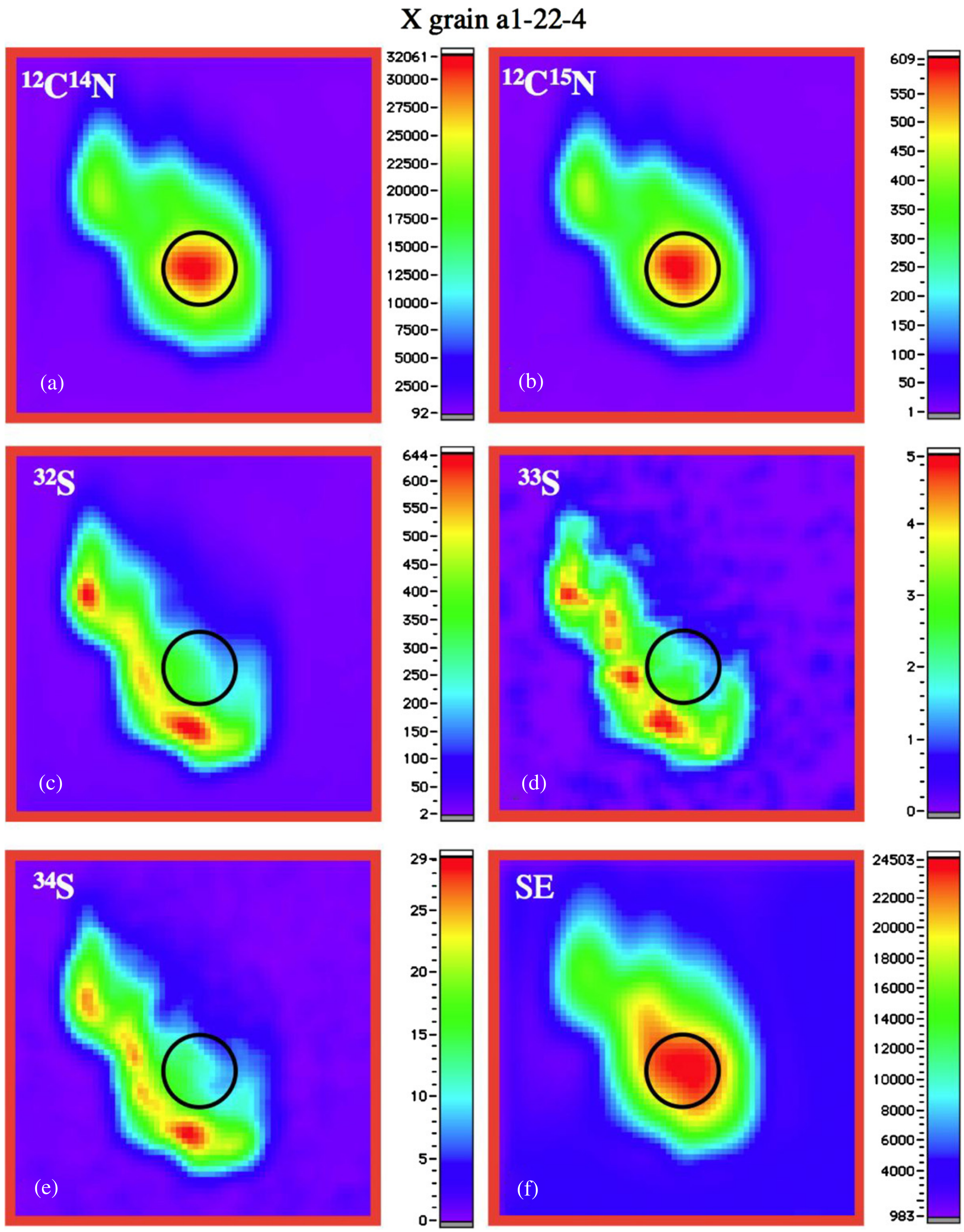

Figure 15. NanoSIMS images of CN and S ions and secondary electrons for the X grain a1–22–4. The images are over a $2 \times 2\ \mu m^2$ area and consist of 64×64 pixels each. The area within the black circle has isotopically anomalous S.

all Z grains of this study and an additional previously studied Z grain require a metallicity of $Z = \sim 0.002$. As explained by Zinner et al. (2006), we account for galactic evolution affecting the initial Si and S isotopic compositions of stars of lower-than-solar metallicity by scaling the heavy isotopes with the Fe abundances and by assuming that the abundances of the α-nuclei ^{28}Si and ^{32}Si increase with decreasing metallicity. For $Z = 0.003$ and $Z = 0.002$, the resulting initial Si and S δ-values are –173‰ and –206‰, respectively. In Figure 18(a) we also plot the predictions by the FRANEC Repository of Updated Isotopic Tables and Yields (FRUITY) models for AGB stars with $M = 2\ M_{\odot}$ and $3\ M_{\odot}$ and $Z = 0.003$ (Cristallo et al. 2011). Not only do the FRUITY models not assume non-solar isotopic ratios for the parent stars, the Si isotopic shifts predicted are much smaller than those predicted by the Torino models, too small to explain the Si isotopic ratios of the Z grains of this study.

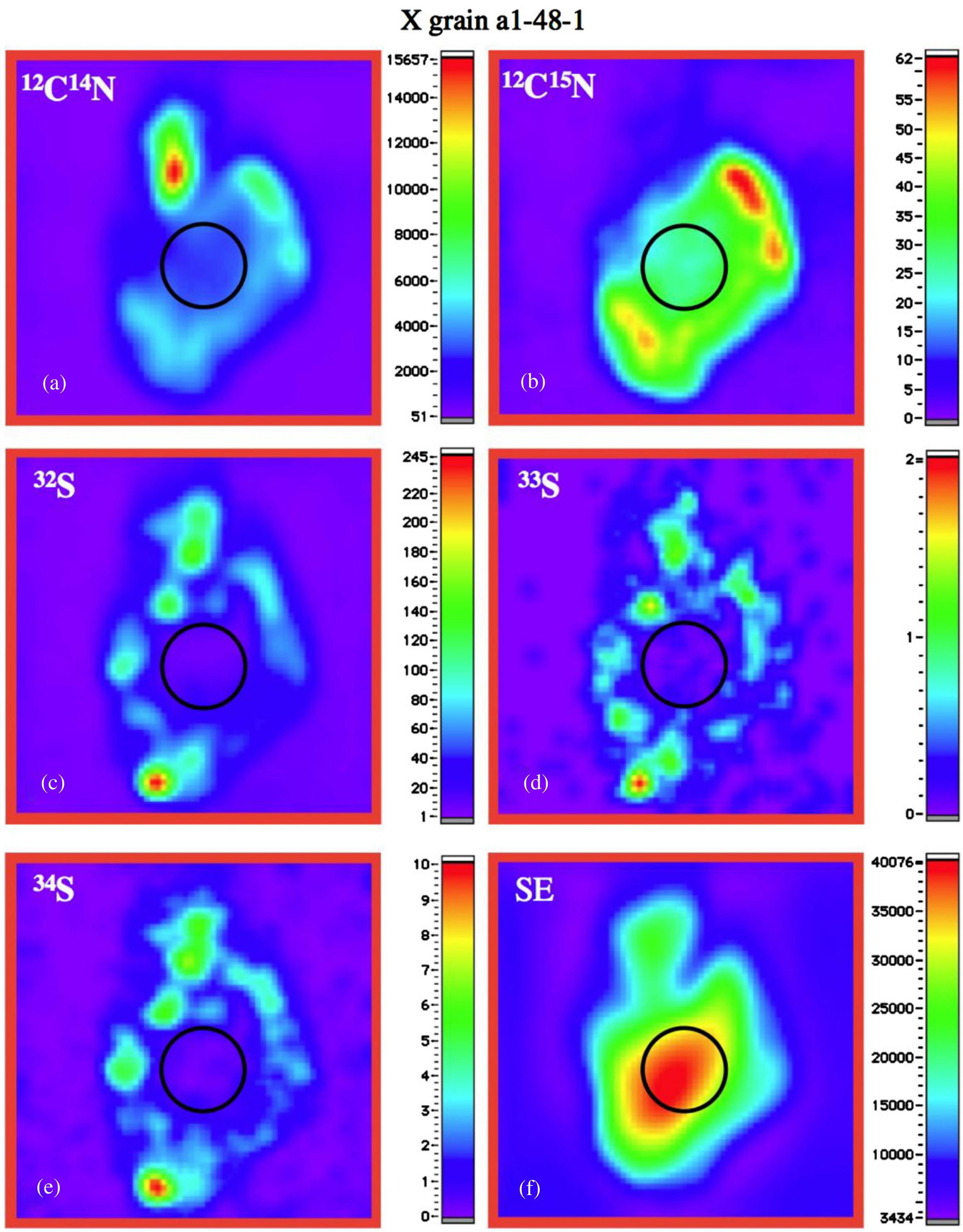

Figure 16. NanoSIMS images of CN and S ions and secondary electrons for the X grain a1–48–1. The images are over a 3 × 3 μm^2 area and consist of 64 × 64 pixels each. The area within the black circles has isotopically anomalous S. Above the main grain is a small attached grain with a high $^{14}N/^{15}N$ ratio (hotspot in panel (a)), most likely a mainstream grain.

In Figure 18(b) we show the AGB predictions for $\delta^{30}Si/^{28}Si$ and $\delta^{34}S/^{32}S$ values of the 3 $M_\odot$, $Z = 0.003$ and $Z = 0.002$ models. The Z grains do not show the moderate ^{34}S excesses expected to correspond to their ^{30}Si excesses. In Figure 18(c) we show the range of S isotopic ratios that would be predicted to correspond to their ^{30}Si excesses. It is obvious that the measured S isotopic ratios are quite different. While most of the grains have close-to-normal ratios, it is puzzling that all grains have ^{34}S deficits, especially grain a1–17–4, whose low $^{34}S/^{32}S$ ratio cannot be explained by contamination with isotopically normal S.

The ^{30}Si excess of Y grain a1–16–11 is much larger than any of typical Y grains (Amari et al. 2001). An AGB star with $Z = 0.001$ can reproduce the Si isotopic ratios of this grain. For such

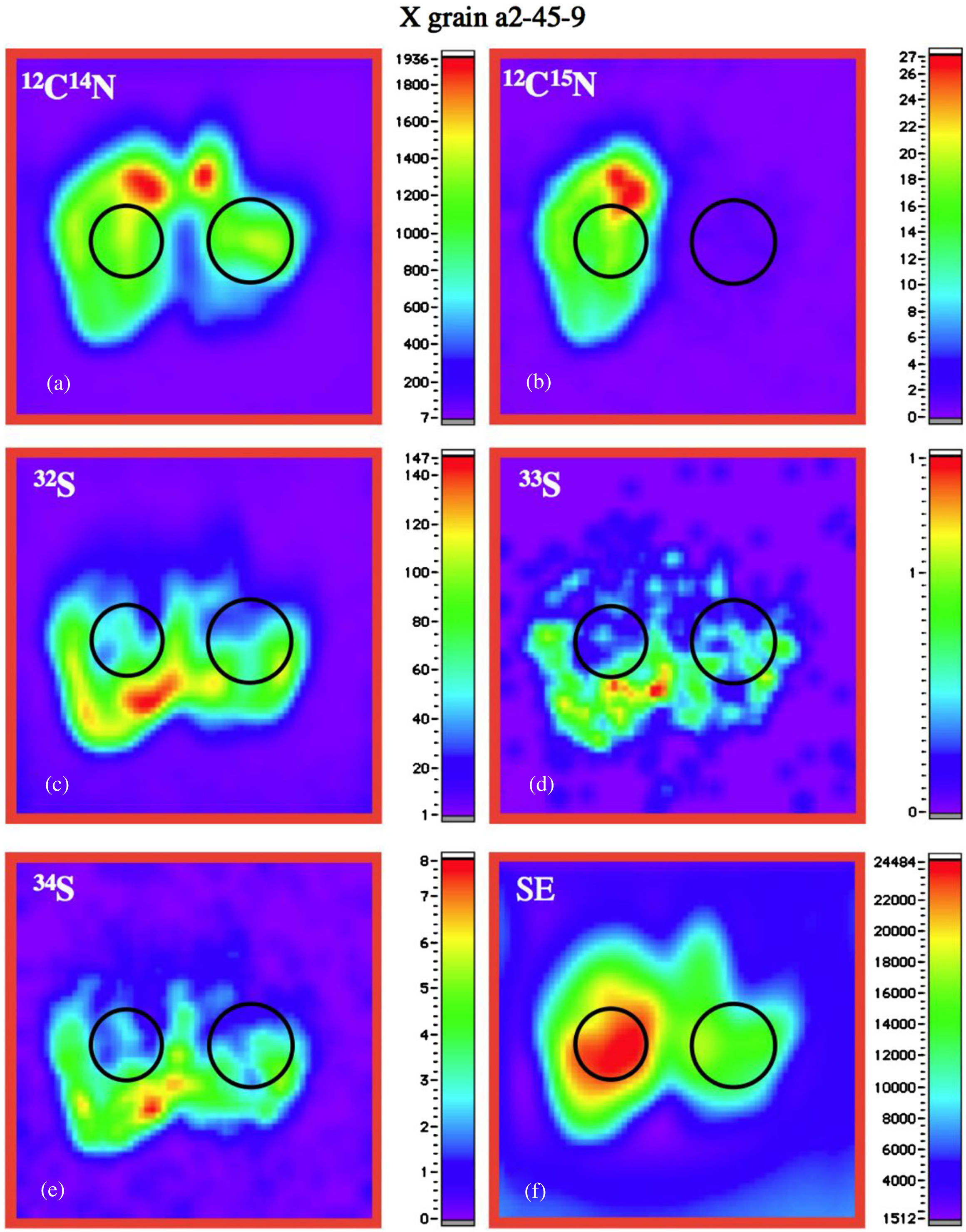

Figure 17. NanoSIMS images of CN and S ions and secondary electrons for the X grain a2–45–9. The images are over a 2.5 × 2.5 μm^2 area and consist of 64 × 64 pixels each. There are two grains in this image: an X grain on the left, and a mainstream grain with a high $^{14}N/^{15}N$ ratio on the right. The area within the left circle has large $^{33,34}S$ deficits, the $^{33,34}S$ deficits in the right circle are marginal.

a star we predict a ^{33}S deficit and ^{34}S excess even larger than the range predicted for the Z grains of this study (Figure 18(c)). Against expectations, the measured S isotopic ratios of this grain are perfectly normal (Table 1 and Figure 1(b)). Again, we have to invoke contamination or isotopic equilibration to explain this result.

Although it is frustrating that the S isotopic ratios of many presolar SiC grains expected to have S isotopic anomalies are close to normal and thus cannot provide much information about their stellar sources, the situation is similar to that presented by the largely normal (terrestrial) N and O isotopic ratios of high-density graphite grains (Jadhav et al. 2013). The large range of C isotopic ratios in these grains implies large anomalies in the N and O isotopic ratios, which, however, are not observed. Similarly, the large Si isotopic anomalies in X, Y, and Z grains imply large S isotopic anomalies, which are not seen. The

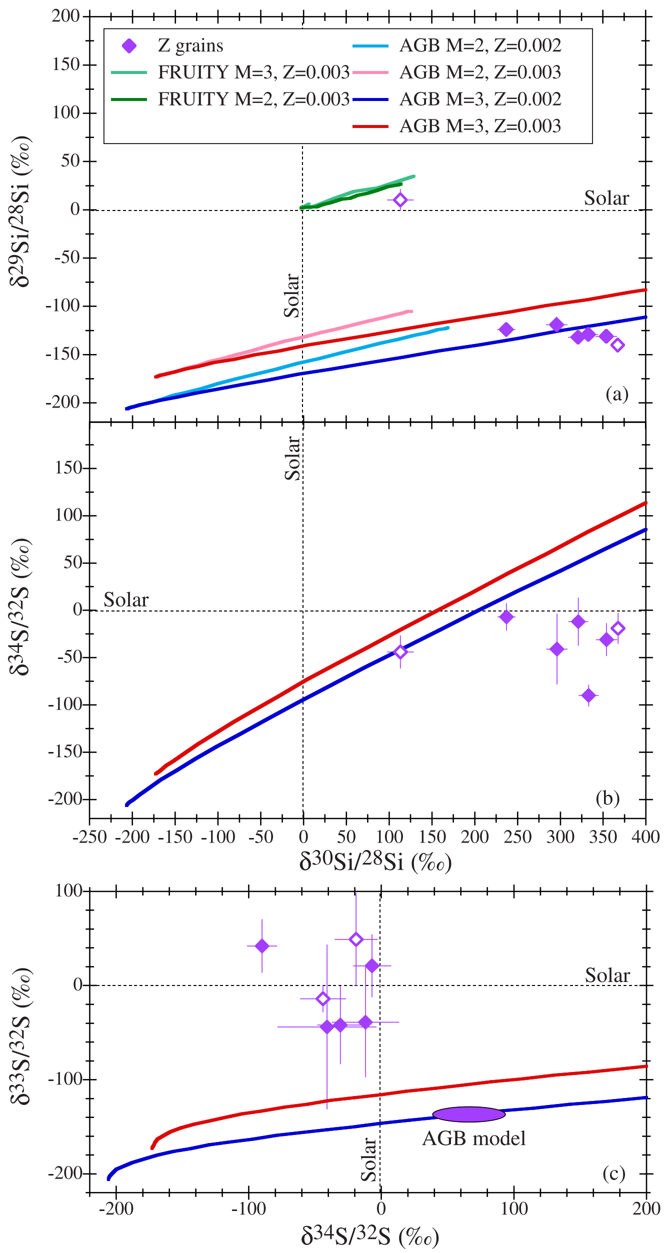

Figure 18. Si and S isotopic ratios of Z grains of this study (solid diamonds) and grains of previous studies whose S isotopes had been analyzed (open diamonds). The blue and red solid lines are predictions by the Torino models (Gallino et al. 1998; Bisterzo et al. 2010) for AGB stars of 2 $M_\odot$ and 3 $M_\odot$ (top panel) and 3 $M_\odot$ (lower panels) and metallicities $Z = 0.002$ and $Z = 0.003$. The green solid lines in panel (a) are predictions by the FRUITY model (Cristallo et al. 2011). The solid ellipse in Figure 6(c) is the range of S isotopic ratios predicted from the Si isotopic ratios of the grains (see text). As can be seen, the measured S isotopic compositions do not agree with these model predictions.

S/Si ratios of Z grains are comparable to those of X grains (Figure 13). As for the X grains, the close-to-normal S isotopic compositions of Z grains are most likely due to contamination with terrestrial S.

4. CONCLUSIONS

1. During a C–Si isotopic automatic-grain-mode search of 1113 presolar SiC grains from the Murchison meteorite we identified 1 C grain, 16 X grains, 1 Y grain, 5 Z grains, and 2 X-type Si_3N_4 grains, which we analyzed in more detail, including S isotopic analyses of all selected grains.
2. The C grain has a large ^{32}S excess, larger than that predicted for the Si/S zone of core–collapse SNe. This is evidence against the fractionation model by Hoppe et al. (2012). A much more likely explanation is a radiogenic origin of the ^{32}S excess from the decay of short-lived ^{32}Si. Both the 12 $M_\odot$ SN model by Woosley & Heger (2007) and the 15r and 15r4 SN models by Pignatari et al. (2013c) have C-rich regions with high ^{32}Si abundances produced by neutron capture at high neutron densities and can explain the ^{32}S excesses together with the large ^{29,30}Si/^{28}Si ratios and the ^{12}C/^{13}C ratios of C grains. The Pignatari et al. model gives a better fit to the ^{29,30}Si/^{28}Si ratios of the C grain. However, it cannot match simultaneously its C and N isotopic ratios. Both models can explain all the other isotopic ratios of the grain. Except for radiogenic ^{32}S, intrinsic S concentrations are extremely low and contamination with isotopically normal S affects the measured ratios.
3. The C, Si, N, inferred ^{26}Al/^{27}Al, and ^{44}Ti/^{48}Ti ratios in X grains are comparable to those found in previous studies. Sulfur isotopic ratios show, on average, ^{32}S excesses, but these are much smaller than expected, and contamination must be invoked to explain the data. The ^{32}S excesses favor conventional SN models with ^{28}Si production by O burning (e.g., Rauscher et al. 2002; Woosley & Heger 2007) over the explosive SN model by Pignatari et al. (2013b) with ^{28}Si production by a chain of α-captures. The 12 $M_\odot$ SN model by Woosley & Heger (2007) also gives a better fit to the N and Al isotopic ratios of the grains than the Pignatari et al. model. On the other hand, the reader should be reminded that the Pignatari et al. (2013b) model avoids the problem with the missing ^{54}Fe excesses in SiC X grain faced by mixing models with the Si/S zone.
4. The extremely large ^{30}Si excesses in the Y and the Z grains of this study imply an origin in low-mass AGB stars with metallicities between 0.001 and 0.002. The S isotopic ratios predicted for such stars are not found in the grains and, again, contamination must be invoked. The relatively low ^{12}C/^{13}C ratios of the grains are explained by extra mixing (cool bottom processing).

Y.X. is grateful to the Laboratory for Space Sciences and the Physics Department of Washington University for their kind and friendly support during all stages of isotopic analysis and data processing. We thank Sachiko Amari for sample preparation, Frank Gyngard for assistance with NanoSIMS analysis, Evan Groopman for help with the AGB models, and Peter Hoppe for providing information on the S/Si ratios in C grains. This work was supported by NASA (grant NNX11AH14G, E.Z.) and the Natural Science Foundation of China (40830421, Y.X. and Y.L.). A.H. was supported by an ARC Future Fellowship (FT120100363). M.P. acknowledges the support to NuGrid from NSF grants PHY 02-16783 and PHY 09-22648 (Joint Institute for Nuclear Astrophysics, JINA) and EU MIRG-CT-2006-046520, from the Ambizione grant of the SNSF and the SNF grant 200020-132816 (Switzerland) and Eurogenesis (MASCHE).

REFERENCES

Amari, S., Hoppe, P., Zinner, E., & Lewis, R. S. 1995, Metic, 30, 679
Amari, S., Lewis, R. S., & Anders, E. 1994, GeCoA, 58, 459
Amari, S., Nittler, L. R., Zinner, E., et al. 2001, ApJ, 546, 248
Bao, Z. Y., Beer, H., Käppeler, F., et al. 2000, ADNDT, 76, 70
Bernatowicz, T. J., Amari, S., & Lewis, R. S. 1992, LPSC, 23, 91
Besmehn, A., & Hoppe, P. 2003, GeCoA, 67, 4693

Bisterzo, S., Gallino, R., Straniero, O., Cristallo, S., & Käppeler, F. 2010, MNRAS, 404, 1529
Blake, J. B., & Schramm, D. N. 1976, ApJ, 209, 846
Bojazi, M. J., & Meyer, B. S. 2014, PhRvC, 89, 025807
Clayton, D. D., & Nittler, L. R. 2004, ARA&A, 42, 39
Cristallo, S., Piersanti, L., Straniero, O., et al. 2011, ApJS, 197, 17
Davis, A. M. 2011, PNAS, 108, 19142
Farouqi, K., Kratz, K.-L., & Pfeiffer, B. 2009, PASA, 26, 194
Fryer, C. L., Belczynski, K., Wiktorowicz, G., et al. 2012, ApJ, 749, 91
Gallino, R., Arlandini, C., Busso, M., et al. 1998, ApJ, 497, 388
Grefenstette, B. W., Harrison, F. A., Boggs, S. E., et al. 2014, Natur, 506, 339
Groopman, E., Bernatowicz, T., & Zinner, E. 2012, ApJL, 754, L8 (6pp)
Guber, K. H., Koehler, P. E., Derrien, H., et al. 2003, PhRvC, 67, 062802
Gyngard, F., Amari, S., Zinner, E., & Ott, U. 2009, ApJ, 694, 359
Gyngard, F., Nittler, L. R., & Zinner, E. 2010a, M&PSA, 45, A72
Gyngard, F., Orthous-Daunay, F.-R., Zinner, E., & Moynier, F. 2012, M&PSA, 47, 5255
Gyngard, F., Zinner, E., Nittler, L. R., et al. 2010b, ApJ, 717, 107
Hammer, N. J., Janka, H.-T., & Müller, E. 2010, ApJ, 714, 1371
Henkel, T., Stephan, T., Jessberger, E. K., et al. 2007, M&PS, 42, 1121
Hoppe, P., Fujiya, W., & Zinner, E. 2012, ApJL, 745, L26
Huss, G. R., & Lewis, R. S. 1995, GeCoA, 59, 115
Hynes, K. M., Croat, T. K., Amari, S., Mertz, A. F., & Bernatowicz, T. J. 2010, M&PS, 45, 596
Hynes, K. M., & Gyngard, F. 2009, LPSC, 40, 1198
Iliadis, C., Longland, R., Champagne, A. E., Coc, A., & Fitzgerald, R. 2010, NuPhA, 841, 31
Jadhav, M., Zinner, E., Amari, S., et al. 2013, GeCoA, 113, 193
Joggerst, C. C., Woosley, S. E., & Heger, A. 2009, ApJ, 693, 1780
Kifonidis, K., Plewa, T., Janka, H.-T., & Müller, E. 2003, A&A, 408, 621
Lin, Y. T., Gyngard, F., & Zinner, E. 2010, ApJ, 709, 1157
Lodders, K., & Amari, S. 2005, ChEG, 65, 93
Lugaro, M., Davis, A. M., Gallino, R., et al. 2003, ApJ, 593, 486
Magkotsios, G., Timmes, F. X., Hungerford, A. L., et al. 2010, ApJS, 191, 66
Marhas, K. K., Amari, S., Gyngard, F., Zinner, E., & Gallino, R. 2008, ApJ, 689, 622
Messenger, S., Keller, L. P., Stadermann, F. J., Walker, R. M., & Zinner, E. 2003, Sci, 300, 105
Meyer, B. S., & Bojazi, M. J. 2011, LPSC, 42, 2376
Meyer, B. S., Clayton, D. D., & The, L. S. 2000, ApJL, 540, L49
Meyer, B. S., Weaver, T. A., & Woosley, S. E. 1995, Metic, 30, 325
Müller, E., Fryxell, B., & Arnett, D. 1991, A&A, 251, 505
Nittler, L. R. 2003, E&PSL, 209, 259
Nittler, L. R., & Hoppe, P. 2005, ApJL, 631, L89
Orthous-Daunay, F.-R., Gyngard, F., Moynier, F., & Zinner, E. 2012, LPSC, 43, 2697
Pellin, M. J., Davis, A. M., Lewis, R. S., Amari, S., & Clayton, R. N. 1999, LPSC, 30, 1969
Pignatari, M., Herwig, F., Hirschi, F., et al. 2013a, arXiv1307.6961P
Pignatari, M., Wiescher, M., Timmes, F. X., et al. 2013b, ApJL, 767, L22
Pignatari, M., Zinner, E., Bertolli, M. G., et al. 2013c, ApJL, 771, L7
Rauscher, T., Heger, A., Hoffman, R. D., & Woosley, S. E. 2002, ApJ, 576, 323
Slodzian, G., Hillion, F., Stadermann, F. J., & Zinner, E. 2004, ApSS, 231, 874
Stadermann, F. J., Hoppe, P., Floss, C., et al. 2008, M&PS, 43, 299
Timmes, F. X., Woosley, S. E., Hartmann, D. H., & Hoffman, R. D. 1996, ApJ, 464, 332
Travaglio, C., Gallino, R., Amari, S., et al. 1999, ApJ, 510, 325
Woosley, S. E., & Heger, A. 2007, PhR, 442, 269
Woosley, S. E., Heger, A., Cumming, A., et al. 2004, ApJS, 151, 75
Woosley, S. E., & Weaver, T. A. 1995, ApJS, 101, 181
Xu, Y. C., Amari, S., Gyngard, F., Zinner, E., & Lin, Y. 2012, M&PS, 47, 5104
Yada, T., Floss, C., Stadermann, F. J., et al. 2008, M&PS, 43, 1287
Yoshida, T. 2007, ApJ, 666, 1048
Zinner, E. 2014, in Treatise on Geochemistry Vol 1.4, ed. H. D. Holland, K. K. Turekian, & A. Davis (2nd ed.; Oxford: Elsevier), 181
Zinner, E., Amari, S., Guinness, R., et al. 2007, GeCoA, 71, 4786
Zinner, E., & Jadhav, M. 2013, ApJ, 768, 100
Zinner, E., Jadhav, M., Gyngard, F., & Nittler, L. R. 2011, LPSC, 42, 1070
Zinner, E., Nittler, L. R., Gallino, R., et al. 2006, ApJ, 650, 350